DEVELOPING COMPUTATIONAL MODELS FOR PULSED-INDUCTIVE PLASMA FORMATION

by

ZACHARY AARON GILL

A THESIS

Presented to the Graduate Faculty of the

MISSOURI UNIVERSITY OF SCIENCE AND TECHNOLOGY

In Partial Fulfillment of the Requirements for the Degree

MASTER OF SCIENCE

in

AEROSPACE ENGINEERING

2018

Approved by

Dr. Joshua Rovey, Co-Advisor
Dr. Daoru Han, Co-Advisor
Dr. Serhat Hosder

ABSTRACT

Pulsed-inductive discharges are a common method of producing a plasma. They provide a mechanism for quickly and efficiently generating a large volume of plasma for rapid use and are seen in applications including propulsion, fusion power, and high-power lasers. However, some common designs see a delayed response time due to the plasma forming when the magnitude of the magnetic field in the device is at a minimum. New designs are difficult to evaluate due to the amount of time needed to construct a new geometry and the high monetary cost of changing the power generation circuit. To more quickly evaluate new designs and better understand the shortcomings of existing designs, two computational models have been developed for use in Mathematica. The first model uses a modified single-electron model to determine how the energy distribution in a system changes with regards to time and location. The second model uses Townsend breakdown to obtain the time rate of change of electron number density. This rate is then integrated to obtain an electron number density distribution that varies with regards to time and location. By analyzing the energy distribution and the density distribution, the approximate times and locations of initial plasma breakdown and bulk plasma formation can be predicted. The results from these codes are then compared to existing data to show their validity and shortcomings.

ACKNOWLEDGMENTS

I would first like to thank Dr. Joshua Rovey and Dr. Daoru Han for giving me a chance and taking me on as a graduate student. The experiences I have gained under their guidance will serve me for a lifetime. I would also like to thank Dr. F. Scott Miller for his help with using CASINO. I would like to thank Dr. Serhat Hosder for serving on my committee and helping me to receive my Master's degree. I would like to thank Dr. David Riggins for being a voice of reason in both my personal and professional lives. In addition, I would like to thank the Missouri University of Science and Technology for their support of my education in Rolla via the Chancellor's Distinguished Fellowship.

I would like to thank my friends in the Aerospace Plasma Lab for their support. They kept me focused when the going got tough and were quick to provide an honest and helpful answer when I came to them with questions.

Lastly, I would like to thank my family for always being there for me. I absolutely could not have made it through these past few years without them.

TABLE OF CONTENTS

Page

LIST OF ILLUSTRATIONS

Figure Page

LIST OF TABLES

Table Page

1. INTRODUCTION

1.1. BACKGROUND

There are a variety of mechanisms by which a plasma might form. In the case of an inductively-coupled plasma, the primary mechanism is ionization resulting from high-energy collisions between neutral gas particles and free electrons. These free electrons are naturally present in any gas due to background radiation but have neither the energy nor the numbers to produce a plasma. With too little energy, they still have collisions but are repelled and only minimally perturb the neutral gas particles. An electric field can be applied to the gas that accelerates the electrons to energies sufficient for ionizing collisions. These collision knock electrons off of the valence shells of gas atoms, producing both negatively-charged free electrons and positively-charged ions. The new free electrons then go on to conduct even more ionizing collisions. The result is a chain reaction that fills the gas with a cloud of electrons and ions collectively described as a plasma.

1.1.1. Townsend Breakdown. For nearly as long as plasmas have been studied, attempts have been made to quantify their behavior. The most successful model has been the Townsend Breakdown model which describes the electric current between two parallel plates when breakdown occurs. A sketch of the geometry is shown in Figure 1.1.

Initially, this model was a simple exponential model describing the ratio of the measured current I to the photoelectric current I_o due to the electric field strength $\vec{E}$, background gas pressure P, and plate separation d [1]. The model is given in Eqn. (1.1). The electric field and the gas pressure are included by means of the "First Townsend Ionization Coefficient" α.

$$\frac{I}{I_o} = e^{\alpha d} \tag{1.1}$$

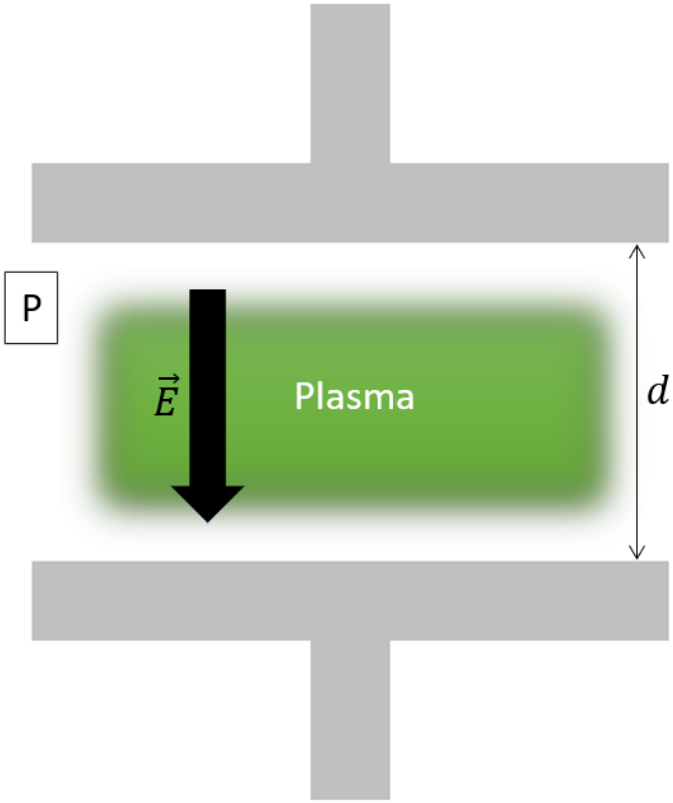

Figure 1.1. Townsend parallel plate geometry.

This coefficient was originally determined empirically for individual experimental setups but an equation relating it the the electric field, gas species, and pressure was developed and presented by Cobine [2]. His equation relied on empirical constants derived for individual gas species over a range of electric field and pressure values. More recently, equations have been developed that relate those constants to fundamental atomic and molecular values [3].

Initial comparisons between Townsend's model an experimental results found that it made accurate predictions for the current only within a limited range of the pertinent conditions. Outside that range, the measured current would be higher than predicted. The cause for the higher current was determined to be additional electrons produced by high energy ions colliding with the cathode [4]. To account for these "secondary electrons" being

emitted by the cathode, a modification was made to Townsend's original model by adding the "Second Townsend Ionization Coefficient," or β. The modified breakdown equation is shown in Eqn. (1.2).

$$\frac{I}{I_o} = \frac{(\alpha - \beta)e^{\alpha d}}{\alpha - \beta e^{\alpha d}} \tag{1.2}$$

Following this modification, the model remained unchanged for decades. More recently, a proposal has been made that suggests the Second Townsend Ionization Coefficient be modified to account for the initial distance traveled by secondary electrons before they can contribute to ionization [5]. Even with the addition of the second term, the Townsend Breakdown model still possesses two limits. First, the model only applies to a parallel-plate geometry with a time-invariant electric field and no magnetic field. Second, it only applies to low-current breakdown, the so-called Townsend Regime.

Soon after the Townsend Breakdown Model was established, efforts were made to understand how it could be modified to account for the presence of a magnetic field. Some of these early works were detailed by Blevin where the magnetic field is specifically a direct current (DC) field perpendicular to the electric field [6]. Two key modifications were discussed: the first being an effective pressure term that relates the system with a magnetic field to an equivalent system with a different pressure and no magnetic field and the second being a reevaluation of the energy gained by a free electron between individual collisions with neutral gas particles. In both cases, Blevin identified that while the models did bear qualitative agreement with experimental work, they did not agree quantitatively. He ultimately concluded that the use of equivalent pressure gave the more accurate results but that secondary ionization, which had previously been assumed unaffected, was indeed affected by the presence of a magnetic field. The model for equivalent pressure described by Blevin was followed up by Sen who determined the effective range of electric field strengths and pressures over which the equivalent pressure term was valid [7]. However, as with the previous results by Blevin, Sen acknowledged that accounting for changes to the

secondary ionization coefficient due to strong magnetic fields would provide more accurate results. This work was later followed up on by Haydon who demonstrated that the electron energy distribution experienced fundamental changes when put under a magnetic field [8]. Specifically, Haydon demonstrated that the energy distribution was no longer Maxwellian when a magnetic field was present. Thus, an equivalent distribution without a magnetic field could not be determined. He proposed modifying the previously developed equivalent pressure term with an empirical multiplier to account for the change in energy distribution. For nearly 50 years after Blevin's work, no efforts were made to follow up on his suggestion to change the second coefficient. Finally, a study published by Radmilovic-Radjenovic in 2006 proposed some possible changes [9]. In particular, the study focused both on how the magnetic field can affect ionic energy and on how gyromotion can force emitted electrons back into the cathode.

1.1.2. AC Breakdown. Given the limited purview of Townsend's model, attempts have been made to develop models for other kinds of plasma discharges. A broad class of plasmas that has seen much modeling work is the plasmas produced by an alternating current (AC) electric field. Unlike a DC electric field, an AC electric field varies with time such that a magnetic field will form as described by the Maxwell-Ampère Equation. A common example of a plasma formed under an AC electric field is the radio-frequency (RF) plasma. RF plasmas, steady-state plasmas produced by fields typically with a frequency of 13.56 MHz, have seen widespread use in industrial, commercial, and academic fields. The most common variant of the RF plasma is the capacitively-coupled plasma (CCP), a plasma formed between two electrodes similar to the parallel plate geometry used in Townsend Breakdown. A less common but still important variant of the RF plasma is the inductively-coupled plasma (ICP). Where CCPs are formed between electrodes, ICPs are formed in the presence of an inductive coil. A comprehensive model for both ICPs and CCPs was produced by Chabert and Braithwaite [10]. The models presented in their book were designed primarily for Argon and focus on steady-state plasma conditions. However, some

commentary was provided for conditions necessary to achieving initial plasma formation. A standard means of accounting for the presence of a magnetic field is to ignore gyromotion induced in the ions and instead focus on drift motion such as that used by Chen to describe a Helicon plasma [11]. A similar method is to average the particle motion and interactions over time such as that used by Tarvainen to describe an Electron Cyclotron Resonance (ECR) plasma [12]. These methods are only valid for their respective cases because the gas breakdown occurs on a longer time-scale than the oscillation of the magnetic field. In the model presented by Tarvainen, the ECR plasma forms on the scale of hundreds of microseconds for a magnetic field frequency on the scale of a GHz [12]. In the example illustrated by Chen, the focus is on long-term equilibrium for a helicon plasma at which point the rate of formation will equal the loss rate [11]. In fact, equilibrium is a fairly common approach to modeling plasma formation. This approach equates formation to stability by stating that a plasma will only form if its creation rate equals its loss rate. A standard visualization of this approach is the Paschen curve where the curve represents the values of gas pressure and electric field at which breakdown becomes possible. There are two issues with this type of approach. First, it only looks at whether a plasma will eventually form. It ignores the particulars of when and where in a geometry such formation happens. In Chen's model for a Helicon plasma, he noted his surprise at the plasma remaining confined to a small region near the axis rather than being uniformly distributed [11]. The second issue with using equilibrium conditions is that they are only applicable for fields that remain stable over a long period of time. Thus, the time scale on which the fields evolve can be assumed to be much larger than the time scale on which the plasma forms. An example of this for an AC field is a model developed by Burm to determine breakdown conditions for ICPs [13]. This model applied Townsend Breakdown to a plasma confined in a solenoid. The driving force of the magnetic field was accounted for by using Faraday's Law to relate the magnetic field to the electric field and thereby replace the electric field in the Townsend Breakdown model with the magnetic field. Because the fields experienced little to no

decay, the model was able to use magnitudes of the electric and magnetic fields rather than time-varying quantities. Specifically, the electric field was related to the magnetic field as $E = \omega BR$ where ω was the angular frequency of the magnetic field and R was the radius of the chamber. The value of the first ionization coefficient used by the model was the original term developed by Cobine that ignored any influence from the magnetic field outside of inducing the electric field. The ignorance of modifications to the first coefficient by the magnetic field may be valid as the fields in this case were coupled.

1.2. INDUCTIVELY-COUPLED PLASMA

ICPs are a class of magnetically-coupled plasmas that include ECR plasmas, Surface-Wave Plasmas (SWP), and Helicon plasmas. Their collective value over Capacitively-Coupled Plasmas (CCP) is twofold. First, they have a reduced or even no reliance on electrodes, thus significantly increasing the lifespan of the device producing the plasma. Second, they can produce plasmas of much higher density [11] [14] [15]. Due to these advantages, ICPs have been used in a wide range of applications. They have been used in material fabrication to provide high-fidelity etching [16] [17] and to modify materials to be hydrophilic [18]. They have also been used to study fusion plasmas. Magnetic-confinement fusion is predicated on using magnetic fields to either radially or axially confine a plasma. The resultant configurations typically mimic those of ICPs and are generally called Field-Reversed Configuration (FRC) plasmas. Thus, ICPs are used to develop better confinement and ignition methods [19] [20] [21] [22] [23]. A third application for ICPs is space-based propulsion. Space-based systems cannot be easily repaired or replaced which makes the long lifespans inherent in ICP devices advantageous. Various space-based propulsion systems that have made use of ICPs as their propellant include the electrodeless Lorentz Force (ELF) thruster [24], the Pulsed-Inductive Thruster (PIT) [25], the Inductive Pulsed Plasma Thruster (IPPT) [26], and the Nuclear-Electric PIT (NuPIT) [27].

A variant of the ICP that has proven notorious to model is the pulsed-inductive plasma (PIP). Unlike standard ICPs that oscillate in continuous wave (cw) form, PIPs are formed by fields that are pulsed; that is, they are generated for a short period of time before decaying away. The benefit of PIPs over other ICPs is their ability to rapidly and repeatedly produce plasma for recurring use. Previous work had shown that plasma formation is driven primarily by power with a qualitative attachment to the azimuthal electric field [28]. However, more recent work has shown that plasma formation is not tied to peaking of the electric field, when power transfer would be at a maximum, but rather to a zero crossing of the magnetic field [29] [30]. In practice, this coupling has the effect of delaying plasma formation and reducing the initial magnetic field present in the plasma when it forms. As there is little to no magnetic field in the plasma, some time is needed after formation for a magnetic field to spread throughout the medium. Only after the plasma exhibits a magnetic field can it be acted on by electromotive forces and thus generate thrust. The absence of a credible model to explain this phenomenon is one this work seeks to rectify.

1.3. OBJECTIVES OF THIS THESIS

The primary goal of this work is to develop computational models for describing formation of ICPs. To accomplish this goal, a method for deriving the electric and magnetic fields in any ICP device will be developed. The second goal of this work is to obtain agreement between these models and experimental results for various ICP devices.

1.4. ORGANIZATION OF THIS THESIS

First, Section 2 will derive a model for the electric and magnetic fields whereby they can be calculated for any ICP device given the geometry and the electric current waveform. Next, models will be developed that describe plasma formation as a result of (a) energy gain of a single particle in Section 3 and (b) Townsend breakdown in Section

4. Finally, the models will be applied to three different ICP devices: the Missouri Plasma Experiment (MPX) in Section 5, the Field-Reversed Configuration Heating Experiment (FRCHX) in Section 6, and the Conical Theta Pinch - Faraday Acceleration with Radio-frequency Assisted Discharge (CTP-FARAD) in Section 7.

2. MODEL DEVELOPMENT

2.1. GOVERNING EQUATIONS

Any characterization of the action of charged particles must begin with a characterization of the electric and magnetic fields in the region of interest. Using the Lorenz gauge, the fields can be stated using the scalar and vector potentials as shown in Eqns. (2.1) and (2.2). The key condition of the Lorenz gauge is that $\nabla \cdot \vec{A} = 0$. ∇ is nabla, or the del operator. The partial derivative with respect to time is given as ∂_t. $\vec{A}$ is the vector potential. Φ is the scalar potential. $\vec{E}$ is the electric field in a vacuum. $\vec{B}$ is the magnetic field in a vacuum.

$$\vec{E} = -\nabla \cdot \Phi - \partial_t \vec{A} \tag{2.1}$$

$$\vec{B} = \nabla \times \vec{A} \tag{2.2}$$

2.2. ELECTROMAGNETIC FIELDS

Gauss's Law can be used to derive Poisson's equation from Eqn. (2.1). Gauss's Law is given in Eqn. (2.3). ρ is the spatial charge density and ϵ_o is the vacuum permittivity. Taking the divergence of both sides of Eqn. (2.1) gives Eqn. (2.4). Setting Eqn. (2.3) equal to Eqn. (2.4) and recalling that $\nabla \cdot \vec{A} = 0$ for the Lorenz gauge results in Eqn. (2.5), or Poisson's equation. In the case that there is no charge density in the region of interest, Poisson's equation simplifies to Laplace's equation, Eqn. (2.6).

$$\nabla \cdot \vec{E} = \frac{\rho}{\epsilon_o} \tag{2.3}$$

$$\nabla \cdot \vec{E} = -\nabla^2 \Phi - \partial_t [\nabla \cdot \vec{A}] \tag{2.4}$$

$$\nabla^2 \Phi = -\frac{\rho}{\epsilon_o} \tag{2.5}$$

$$\nabla^2 \Phi = 0 \tag{2.6}$$

2.2.1. Scalar Potential for a Cylinder. If the region is set to be a cylinder of radius R and the scalar potential is set to be a constant, Φ_o, along the outer surface of the cylinder, that is, at radius R, then the scalar potential throughout the region simplifies to a constant such that the electric field due to it is zero. This derivation is shown below. $\vec{r}$ is the general position vector whereas r without the vector arrow is the radial position, or distance from the central axis. The partial derivative with respect to the radial position is given as ∂_r.

$$\begin{aligned}
\Phi(\vec{r}) &= \Phi(r) \\
\Phi(R) &= \Phi_o \\
\nabla^2 \Phi &= [\partial_r^2 + \frac{1}{r}\partial_r]\Phi \\
&= 0 \\
\partial_r \Phi &= -r\partial_r^2 \Phi \\
\int_0^R \partial_r \Phi dr &= -\int_0^R r\partial_r^2 \Phi dr \\
&= -R\partial_r \Phi|_{r=R} + \int_0^R \partial_r \Phi dr \\
\partial_r \Phi|_{r=R} &= 0
\end{aligned} \tag{2.7}$$

$$
\begin{aligned}
\partial_r^2\Phi &= \frac{d(\partial_r\Phi)}{dr} \\
\partial_r\Phi &= -r\partial_r^2\Phi \\
&= -r\frac{d(\partial_r\Phi)}{dr} \\
\frac{d(\partial_r\Phi)}{\partial_r\Phi} &= -\frac{dr}{r} \\
\ln(\partial_r\Phi) &= \ln r + C \\
\partial_r\Phi &= e^C r \\
\partial_r\Phi|_{r=R} &= e^C R = 0 \\
e^C &= 0 \\
\partial_r\Phi &= 0 \\
\Phi(r) &= \Phi_o
\end{aligned}
\tag{2.8}
$$

To summarize, the scalar potential is only a function of r such that it exhibits radial symmetry for every possible value of R. Due to this radial symmetry and the lack of any charge in the region, the gradient of the scalar potential becomes zero at the edge of the cylinder. Furthermore, the gradient of the scalar potential is shown to be zero throughout the entire region. Thus, the scalar potential is a constant throughout the region. As a result, $\nabla\Phi = 0$ and Eqn. (2.1) simplifies to Eqn. (2.9).

$$\vec{E} = -\partial_t\vec{A} \tag{2.9}$$

2.2.2. Vector Potential for a Cylinder. The vector potential, $\vec{A}$, present in Eqns. (2.2) and (2.9) can be calculated from the current density of the geometry using Eqn. (2.10). $\vec{J}$ is the current density and μ_o is the vacuum permeability. The time is denoted as t. Typically, this equation uses retarded time rather than real time but the difference will be

treated as negligible for the purposes of this work as the related geometries are too small and the time scale of the applied current is too large for a delay due to the speed of light to be meaningful. The primed terms, such as $\vec{r}'$, are distinct from the unprimed terms, such as $\vec{r}$, in that they are what the integral, via d^3r', integrates over.

$$\vec{A}(\vec{r}) = \frac{\mu_o}{4\pi} \int \frac{\vec{J}(\vec{r}', t)}{|\vec{r} - \vec{r}'|} d^3r' \tag{2.10}$$

The form for the vector potential given in Eqn. (2.10) can be substituted into the previously determined equations for the electric and magnetic fields, Eqns. (2.2) and (2.9), to get the integral forms shown in Eqns. (2.11) and (2.12). In Eqn. (2.11), ∇ is unprimed and thus only operates on the denominator as it contains an unprimed $\vec{r}$.

$$\vec{B} = \frac{\mu_o}{4\pi} \int \nabla \times \frac{\vec{J}(\vec{r}', t)}{|\vec{r} - \vec{r}'|} d^3r' \tag{2.11}$$

$$\vec{E} = -\frac{\mu_o}{4\pi} \int \frac{\partial_t \vec{J}(\vec{r}', t)}{|\vec{r} - \vec{r}'|} d^3r' \tag{2.12}$$

2.2.3. Current Density for a Cylinder. In the event that the geometry is encased in a cylindrical solenoid, the applied current density becomes purely azimuthal. Furthermore, as the shape of the solenoid does not change with time, the current density can be separated into a product of two functions, $I(t)$ and $f(\vec{r}')$. $I(t)$ is the waveform of the electric current. $f(\vec{r}')$ is the spatial density function of the current. The equation for the current density is shown in Eqn. (2.13).

$$\vec{J}(\vec{r}', t) = I(t) f(\vec{r}') \hat{\phi}' \tag{2.13}$$

Eqn. (2.13) can be substituted in place of $\vec{J}$ in the integral forms for the electric and magnetic fields, Eqns. (2.12) and (2.11), to separate $\vec{r'}$ from t and obtain a vector direction for ∇ to operate on. The end result is shown in Eqns. (2.15) and (2.14).

$$\vec{B} = \frac{\mu_o}{4\pi} I(t) \int \nabla \times \frac{f(\vec{r'})\hat{\phi'}}{|\vec{r} - \vec{r'}|} d^3 r' \tag{2.14}$$

$$\vec{E} = -\frac{\mu_o}{4\pi} \partial_t I(t) \int \frac{f(\vec{r'})\hat{\phi'}}{|\vec{r} - \vec{r'}|} d^3 r' \tag{2.15}$$

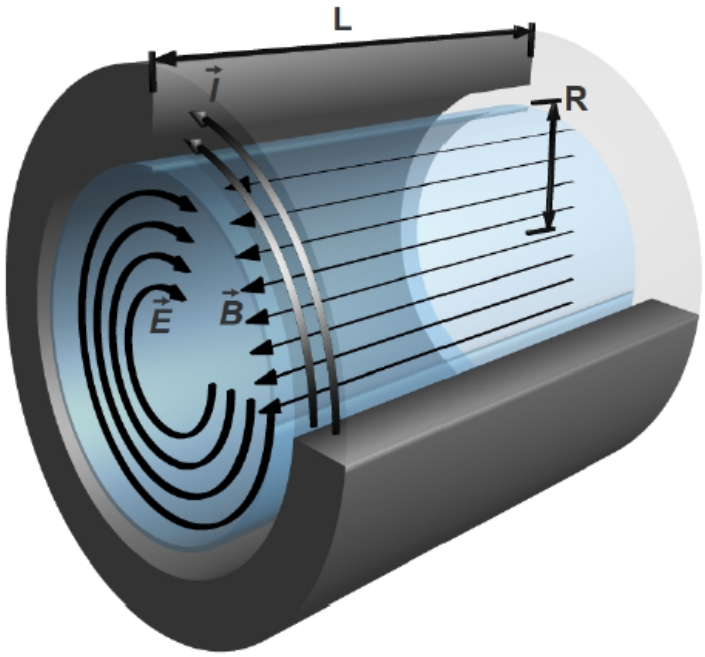

Figure 2.1. Electric and magnetic fields in cylindrical theta pinch. [30]

As the current is assumed to be delivered by means of a cylindrical solenoid, such as a theta pinch, the spatial density function, $f(\vec{r'})$, can be written as Eqn. (2.16) where R is the radius of the solenoid and L is the length. A model depicting how the fields will be arranged in such a system is shown in Figure 2.1.

$$f(\vec{r}') = \frac{\delta(r' - R)}{L} \tag{2.16}$$

$\delta(r' - R)$ indicates that the current is located only at radial position $r' = R$ and the denominator L indicates that the current is distributed evenly along the length of the cylinder. To minimize edge effects, the fields will be calculated at the center of the cylinder. The boundary values will be set to $0 \leq \phi' \leq 2\pi$ to integrate over the entire circumference of the cylinder, $-\frac{L}{2} \leq z' \leq \frac{L}{2}$ to integrate over the entire length of the cylinder and to set the origin at the center of the cylinder, and $0 \leq r' \leq \infty$ to include any possible value of R. The integrals previously given in Eqns. (2.15) and (2.14) can thus be expanded into Eqns. (2.18) and (2.17) for a cylindrical solenoid.

$$\vec{B} = -\frac{\mu_o}{4\pi}\frac{1}{L}I(t)\int_0^{2\pi}\int_{-\frac{L}{2}}^{\frac{L}{2}}\int_0^{\infty} \nabla \times \frac{\delta(r' - R)}{|\vec{r} - \vec{r}'|}\hat{\phi}' r' dr' dz' d\phi' \tag{2.17}$$

$$\vec{E} = -\frac{\mu_o}{4\pi}\frac{1}{L}\partial_t I(t)\int_0^{2\pi}\int_{-\frac{L}{2}}^{\frac{L}{2}}\int_0^{\infty} \frac{\delta(r' - R)}{|\vec{r} - \vec{r}'|}\hat{\phi}' r' dr' dz' d\phi' \tag{2.18}$$

2.3. INTEGRATION OF THE ELECTROMAGNETIC FIELDS

Before values for $\vec{B}$ and $\vec{E}$ can be obtained, a few assumptions must first be made. First, as a cylinder exhibits radial symmetry, the radial position vector $\vec{r}$ can be arbitrarily set parallel to the Cartesian unit vector $\hat{x}$. This arrangement means that the radial unit vector $\hat{r}$ will be equal to the Cartesian unit vector $\hat{x}$ and that the polar unit vector $\hat{\phi}$ will be parallel to the Cartesian unit vector $\hat{y}$. The result of this arrangement is that the denominator in Eqns. (2.17) and (2.18) can be expanded and that the primed unit vectors can be written in terms of the unprimed unit vectors as shown in Eqns. (2.19).

$$\begin{aligned}
\vec{r} &= r\hat{x}, \hat{r} = \hat{x}, \hat{\phi} = \hat{y} \\
\vec{r'} &= r' \cos\phi' \hat{x} + r' \sin\phi' \hat{y} \\
\hat{r'} &= \cos\phi' \hat{x} + \sin\phi' \hat{y} \\
\hat{\phi'} &= -\sin\phi' \hat{x} + \cos\phi' \hat{y} \\
|\vec{r} - \vec{r'}| &= \sqrt{r^2 + r'^2 - 2rr' \cos\phi' + (z - z')^2}
\end{aligned} \tag{2.19}$$

Recall that ∇ from Eqn. (2.17) is not primed meaning that it acts only on unprimed terms, not primed terms. As the unit vector in Eqn. (2.17), $\hat{\phi'}$, is primed, a conversion is needed to relate it to unprimed unit vectors so that ∇ can be properly applied. $\hat{\phi'}$ is converted to the Cartesian coordinate system as shown in Eqn. (2.20). For reasons that will be made apparent, $|\vec{r} - \vec{r'}|$ is included and is converted using the relation shown in Eqns. (2.19). Now that $\hat{\phi'}$ is properly converted, the curl in Eqn. (2.17) can be evaluated to get the result shown in Eqn. (2.21). For reasons that will be made apparent, $|\vec{r} - \vec{r'}|$ is included and is converted using the relation shown in Eqns. (2.19).

$$\frac{\hat{\phi'}}{|\vec{r} - \vec{r'}|} = \frac{-\cos\phi' \hat{x} + \sin\phi' \hat{y}}{\sqrt{(x - r'\cos\phi')^2 + (y - r'\sin\phi')^2 + (z - z')^2}} \tag{2.20}$$

Now that $\hat{\phi'}$ is properly converted, the curl in Eqn. (2.17) can be evaluated to get the result shown in Eqn. (2.21).

$$\nabla \times \frac{\hat{\phi'}}{|\vec{r} - \vec{r'}|} = -\frac{(z - z')\hat{r'} + (x\cos\phi' + y\sin\phi' - r')\hat{z}}{|\vec{r} - \vec{r'}|^3} \tag{2.21}$$

The second assumption is that the radial component $\vec{B}$ is negligible. In practice, it is effectively nonzero only near the ends of the cylinder. This means that the radial component of Eqn. (2.21), the term dependent on $z - z'$, will be ignored.

Recall that the electric current density was separated into functions dependent on time and on position. The same can be applied to the fields. The electric current, $I(t)$, present in Eqns. (2.18) and (2.17), can be separated from the rest of the integral equations. The result is Eqns. (2.22) and (2.23) where F_1 and F_3 are the position-dependent terms, given in Eqns. (2.24) and (2.25).

$$\vec{E} \approx \partial_t I(t) F_1 \hat{\phi} \tag{2.22}$$

$$\vec{B} \approx I(t) F_3 \hat{z} \tag{2.23}$$

$$F_1 = -\frac{\mu_o}{4\pi}\frac{R}{L}\int_0^{2\pi}\int_{-\frac{L}{2}}^{\frac{L}{2}} \frac{\cos\phi'}{\sqrt{r^2+R^2-2rR\cos\phi'+(z-z')^2}} dz'd\phi' \tag{2.24}$$

$$F_3 = -\frac{\mu_o}{4\pi}\frac{R}{L}\int_0^{2\pi}\int_{-\frac{L}{2}}^{\frac{L}{2}} \frac{r\cos\phi' - R}{(r^2+R^2-2rR\cos\phi'+(z-z')^2)^{\frac{3}{2}}} dz'd\phi' \tag{2.25}$$

As a refresher, R and L are the dimensions of the solenoid, μ_o is a constant, the primed terms r' and z' are evaluated by the integrals, and the unprimed terms r and z are the position at which the fields are calculated. A value of $z = 0$ corresponds to an equal distance from both ends of the solenoid and a value of $r = 0$ corresponds to the central axis of the solenoid.

2.4. DISCRETIZATION OF THE ELECTROMAGNETIC FIELDS

The only independent variables needed to calculate the fields are r and z. To expedite the models that will be developed in later chapters, a discrete array of field values can be calculated for a set range of r and z. Recalling Eqns. (2.22) and (2.23), two arrays will be set up that contain calculated values of F_1 and F_3 for specified values of r and z. Along with a defined current waveform, the fields can be approximated for any values of position

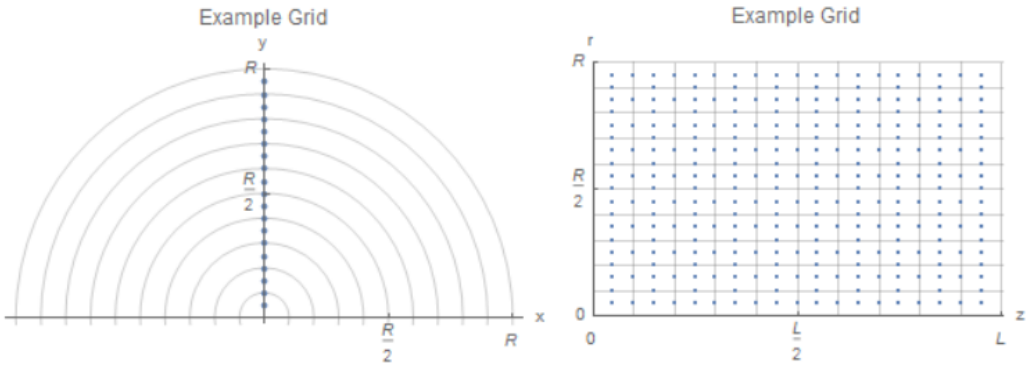

Figure 2.2. Mesh of points at which electric and magnetic fields are calculated.

r and z and time t. An example of how one of these arrays would look laid on top of the model space is shown in Figure 2.2. Note that the xy plot is composed of rings where the only defined boundary is radial. This layout is due to the radial symmetry of the fields within a cylinder. The magnetic field is axial and thus has no x or y components. The electric field is azimuthal and therefore does have x and y components. These components are obtained using the relations shown in Eqns. (2.26). The rz plot is how the xy plot looks from the side. Where the xy plot was divided into rings, the rz plot is divided into cells. The dimensions of the rings and cells will be decided based on accuracy requirements of the individual models. Note that both the rz plot and the xy plot have dots scattered throughout the region. These dots indicate positions where F_1 and F_3 are calculated. Thus, while the fields will be discrete with respect to r and z, they will be continuous with respect to ϕ. The single-particle model will only use the points located at the centers of the rings and cells. The Townsend-breakdown model will use the points both within the rings and cells and at their boundaries.

$$\begin{aligned} \phi &= \arctan[x, y] \\ E_x &= -E \sin\phi \\ E_y &= E \cos\phi \end{aligned} \tag{2.26}$$

3. SINGLE-PARTICLE MODEL

Recall that ICPs typically form due to interactions between free electrons and the neutral gas. The critical term in understanding such formation is the kinetic energy distribution of the free electrons. Previous work conducted by Meeks has shown that plasma formation can be predicted by evaluating the time-evolution of the kinetic energy of a single free electron and equating plasma formation to when the electron's kinetic energy becomes higher than the ionization energy of the gas, or becomes high enough to enable ionizing collisions [30]. His work centered on solving the momentum equation of the electron, given in Eqn. (3.1), and calculating the kinetic energy from the electron's velocity. However, his results relied on spatially-averaged electromagnetic fields and ignored the boundary conditions of the system in question. Furthermore, his work ignored collisions between the electron and the gas. The model presented here accounts for spatial variation of the fields, describes interactions between the electron and the boundary of the system, and presents two separate methods for describing collisions between the electron and neutral gas particles.

$$\partial_t \vec{v} = -\frac{e}{m}(\vec{E} + \vec{v} \times \vec{B}) + \vec{f}_{col} \tag{3.1}$$

3.1. MODELS FOR DESCRIBING COLLISIONS

A simplistic description of the interactions between electrons and neutral gas particles accounts for only two types of collisions: elastic reflective collisions and inelastic ionizing collisions. The latter type has been previously mentioned as being critical to plasma formation. The former type is essential to understanding how a low energy electron moves in a gas. A derivation of how elastic collisions affect low energy electrons has been detailed by Chen [31] and his results are repeated here. The mean free path, λ_{mfp}, is the

average an electron travels before experiencing an elastic collision. It is given in Eqn. (3.2). The first term, n_n, is the number density of the neutral gas particles. It is related to the gas pressure, P, and temperature, T, by the Ideal Gas Law, given in Eqn. (3.3). k is Boltzmann's Constant. The second term in Eqn. (3.2), σ, is the elastic collision cross-section of the gas. It is dependent on the energy of the free electron but is effectively constant for the low energies that this model will be simulating.

$$\lambda_{mfp} = \frac{1}{n_n \sigma} \tag{3.2}$$

$$n_n = \frac{P}{kT} \tag{3.3}$$

The first approach to modeling the elastic collisions experienced by free electrons is the approach used by Chen [31]. This method is to treat the collisions as a constant dampening force that act to drain energy from the electron. For a single particle, the frequency of elastic collisions, γ, is given in Eqn. (3.4) where v is the electron's velocity. This frequency is then related to the collision term in Eqn. (3.1) as shown in Eqn. (3.5). The negative sign just means that the term dampens the velocity. With the appropriate substitutions, the collision term becomes as shown in Eqn. (3.6). Assuming that there is no pressure gradient, P is a constant. Before the plasma forms, there is no significant source of heating for the gas so T will also remain constant. As previously stated, σ is effectively constant. Thus, the only variable term is the velocity, v.

$$\gamma = \frac{v}{\lambda_{mfp}} \tag{3.4}$$

$$\vec{f}_{col} = -\gamma \vec{v} \tag{3.5}$$

$$\vec{f}_{col} = -\frac{P\sigma v}{kT}\vec{v} \tag{3.6}$$

The second model for describing the effect of the elastic collisions is more involved than the first. Rather than numerically integrating a differential equation, the term $\vec{f}_{col}$ is ignored in Eqn. (3.1) and replaced with a piece of code that models each elastic collision individually. The process used in this code is shown in Figure 3.1.

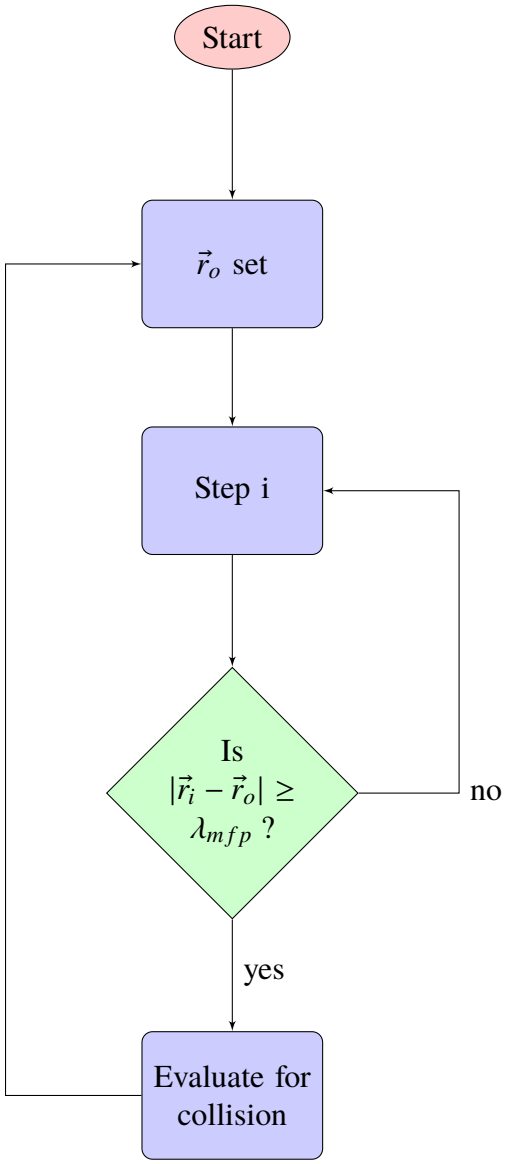

Figure 3.1. Process for calculating Method 2 collisions.

First, a tracker measures the distance the electron has traveled since the last elastic collision. Once the distance becomes greater than or equal to a mean free path length, λ_{mfp} in Eqn. (3.2), a new elastic collision is initiated. The modeled collision is assumed to be head-on such that the electron's velocity is reversed and the speed is reduced by a small amount consistent with the energy that would be lost to the neutral particle. The derivation of this energy loss, performed by Goldston [32], is shown in Eqns. (3.7). The subscript n indicates that the term is for the neutral atom. The subscript e indicates that the term is for the electron. The subscript i indicates that the term is before the collision. The subscript f indicates that the term is after the collision. The resulting energy loss per collision will be very small as it is proportional to the ratio of the two masses.

$$\begin{aligned} mv &\approx MV - mv \\ V &\approx \frac{2mv}{M} \\ \Delta K_n &= \frac{1}{2}MV^2 \\ &\approx \frac{2m^2v^2}{M} \\ &\approx \frac{4m}{M}(\frac{1}{2}mv^2) \\ K_{e,f} &= K_{e,i} - \Delta K_n \\ &\approx K_{e,i}(1 - \frac{4m}{M}) \\ \vec{v}_f &\approx -\vec{v}_i\sqrt{1 - \frac{4m}{M}} \end{aligned} \tag{3.7}$$

3.2. WALL BOUNDARY CONDITIONS

The final component to the single-particle model is modeling the interactions between the free electron and the wall, or boundary, of the region. There are two choices for modeling the wall. They are to (a) model the wall as the surface of a conductor, such as copper, or (b) to model the wall as the surface of a dielectric. If no mention is made

of what material the wall is composed of, the model will default to treating it as a copper conductor. The reasoning for this choice is two-fold. First, electron-surface behavior varies significantly depending on the type of dielectric material in question whereas the behavior of copper is rather straightforward. Second, many pulsed-inductive thrusters such as the PIT [25], the IPPT [26], and certain designs for the CTP-FARAD [33] do not have a dielectric medium between the conductor and the plasma. Copper is typically the conductor used in these devices. If a dielectric medium or a different type of conductor is explicitly identified, then the model can be modified to account for such. As the model will assume that only pre-ionization electrons are present, the surface interactions will be limited to only those of low energy (< 15 eV) electrons.

Gimpel has shown that for low primary energies (< 1 eV) no secondary electrons are produced if the surface is a conductive metal such as copper [34]. This threshold was further extended by Dekker to < 10 eV [35]. As no secondary electrons are produced, all electrons "emitted" by the metal under the threshold are elastically reflected primary electrons. Furthermore, Gimpel determined the reflection coefficient of copper to be $r_e = 0.24$. This reflection coefficient is the ratio of the intensity of electrons reflected by the surface to the intensity of incident electrons. Thus, it gives the fraction of energy not lost to the surface. This reflection coefficient is used in Eqns. (3.8). In multiple studies focusing on electron-metal interactions, it was noticed that contaminated metal surfaces produce a high amount of secondary electrons even at low primary energies [36] [34] [37]. In the case of laboratory plasmas, care is taken to remove contaminations from the system so related secondary emission will be ignored. However, the phenomenon may need further consideration when modeling PIPs used in non-laboratory settings.

In the event that the wall is modeled as a dielectric, properties associated with doing so will be mentioned here. Dekker showed that insulative materials, such as dielectrics, do not uniformly reflect low energy primaries [37]. Instead, the total emission varies strongly with properties of the material in question. He also stated that the surface conditions have

a strong impact on the emission from an insulator [35]. Thus, the working conditions of the PIP and properties associated with the specific material in question would be needed for the model to provide accurate results. A common dielectric that is used as a wall is quartz, or SiO_2. Reflection, or backscattering, behavior was obtained for clean quartz through use of the free software CASINO. For initial energies between 8 eV and 14 eV, the reflected energy was found to be approximately 6.7 eV. The reflection angles were found to be equal to the incident angles for values between 0° and 80°. Simulations of energies lower than 8 eV were unsuccessful as the program would crash before the simulation could finish. As the reflected energy did not vary with the incident energy, quartz will be assumed to output a reflected energy of (a) 6.7 eV if the incident energy is higher or (b) the incident energy if it is lower than 6.7 eV.

As previously stated, the wall by default will be modeled as copper. No secondary electrons will be assumed to form from interactions between the free electron and the wall. When the position of the free electron places it at or beyond the wall, the model code will initiate a wall interaction. The equations describing the interaction are shown in Eqns. (3.8). The subscript i indicates the value before the reflection. The subscript f indicates the value after the reflection. The first two equations depict the conversion of the particle velocities into perpendicular and tangential components. The last two equations depict the original tangential component and the reversed perpendicular component multiplied by the square root of the reflection coefficient being converted back to Cartesian space. As the reflection coefficient r_e was calculated for electron energies, it is therefore proportional to the square of the velocity and thus the velocity is affected by its square root.

$$\begin{aligned} \vec{v}_{\perp} &= v_{x,i}\cos\phi + v_{y,i}\sin\phi \\ \vec{v}_{\parallel} &= -v_{x,i}\sin\phi + v_{y,i}\cos\phi \\ \vec{v}_{x,f} &= -v_{\parallel}\sin\phi - v_{\perp}\sqrt{r_e}\cos\phi \\ \vec{v}_{y,f} &= v_{\parallel}\cos\phi - v_{\perp}\sqrt{r_e}\sin\phi \end{aligned} \tag{3.8}$$

In the event that the wall is quartz, the interaction is as shown in (3.9). Note that the reflection coefficient, r_e, is not present. Instead, a comparison is made between the total velocity, v, and the speed associated with an energy of 6.7 eV, v_Q. If the total velocity is larger than v_Q, then the initial velocities are reduced by a factor of $\frac{v_Q}{v}$.

$$\begin{aligned} v &= \sqrt{v_{x,i}^2 + v_{y,i}^2} \\ v_Q &= \sqrt{\frac{13.4e}{m_e}} \\ \text{If } v > v_Q,\ v_{x,i} &= \frac{v_Q}{v} v_{x,i} \text{ and } v_{y,i} = \frac{v_Q}{v} v_{y,i} \\ \vec{v}_\perp &= v_{x,i} \cos\phi + v_{y,i} \sin\phi \\ \vec{v}_\parallel &= -v_{x,i} \sin\phi + v_{y,i} \cos\phi \\ \vec{v}_{x,f} &= -v_\parallel \sin\phi - v_\perp \cos\phi \\ \vec{v}_{y,f} &= v_\parallel \cos\phi - v_\perp \sin\phi \end{aligned} \tag{3.9}$$

Finally, to account for the distance the electron would have traveled away from the wall after the collision, it is moved to a certain distance, d, inward from the wall. A figure depicting the reflection is shown in Figure 3.2. Equations describing how the displacement due to the reflection is calculated are given in Eqns. (3.10). The angles ϕ and ϕ_o are the position angles of the final position (x_f, y_f) and the initial position (x_i, y_i), respectively. The reflection system is normalized to the initial position vector by setting the base angle to $\phi - \phi_o$. The relations also hold true if the electron is traveling in the opposite direction from what is shown in Figure 3.2.

3.3. PARTICLE PUSHER

Initially, this model performed a simple first-order integration of Eqn. (3.1) to obtain future values of the electron position and velocity. However, that method proved to be fundamentally unstable. The key limiting factor is the magnetic field. Under a magnetic

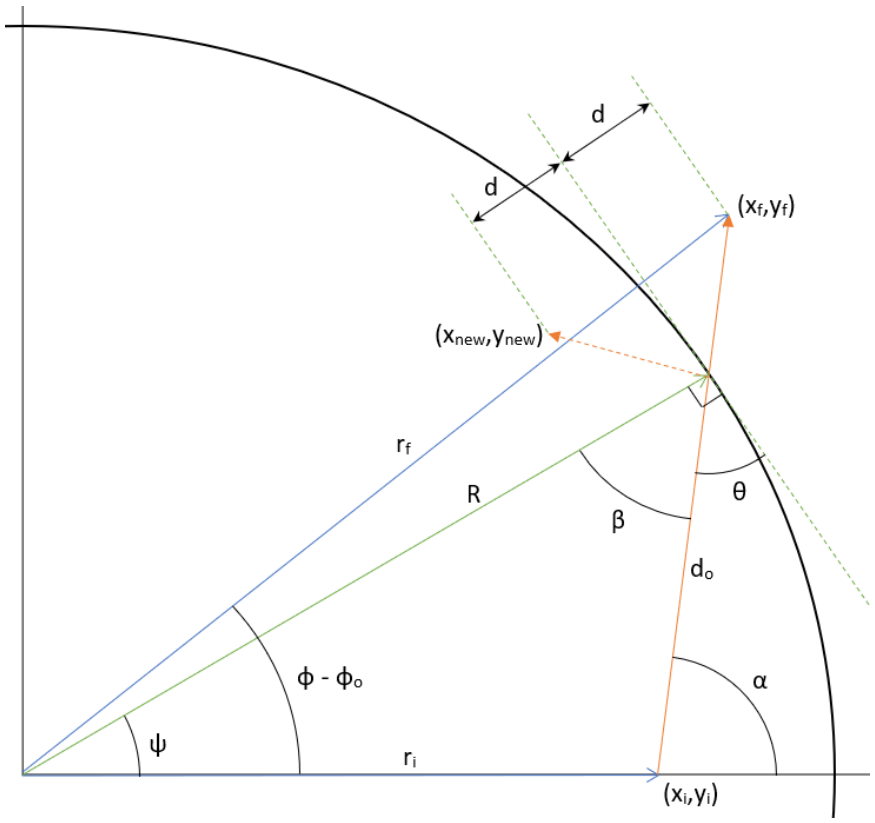

Figure 3.2. Elastic particle reflection on the inner edge of a circular boundary.

field, any charged particle will experience gyromotion. The associated gyroperiod provides an initial limitation on the size of a timestep via $\Delta t_{min} \ll \frac{m}{eB}$. With a small enough timestep, the charged particle will not significantly diverge from expected motion about magnetic field lines. However, increasing the run time or increasing the strength of the magnetic field will severely limit the ability of the model to remain non-divergent. One solution is to use a smaller timestep but this method has the result of increasing the computation cost of the code. A second method is to use an implicit particle pusher such as those used by particle-in-cell (PIC) codes.

$$
\begin{aligned}
r_i &= \sqrt{x_i^2 + y_i^2} \\
r_f &= \sqrt{x_f^2 + y_f^2} \\
d_o &= \sqrt{(x_f - x_i)^2 + (y_f - y_i)^2} \\
\alpha &= \arctan[x_f - x_i, y_f - y_i] \\
\beta &= \arcsin[\frac{r_i r_f}{d_o R} \sin(\phi - \phi_o)] \\
\theta &= \frac{\pi}{2} - \beta \\
\psi &= \alpha - \beta \\
d &= \sqrt{(x - R\cos\psi)^2 + (y - R\sin\psi)^2}\sin\theta \\
x_{new} &= x_f - 2d\cos\psi \\
y_{new} &= y_f - 2d\sin\psi
\end{aligned}
\tag{3.10}
$$

A recent PIC model developed for ICPs by Mattei made use of an implicit routine to counteract divergences due to magnetic fields [38]. Rather than using particle velocities at whole timesteps to move the particle, the model uses an average velocity. As the velocity is integrated linearly between timesteps, this average velocity is assumed to be the particle velocity at the half-timestep between whole timesteps. As the PIC model was developed to model an ICP, it includes parameters that assume a plasma to already be present. Two important inclusions due to this assumption are the addition of a plasma current density and the addition of interactions between ions, electrons, and neutrals. As the single-particle model developed in this paper assumes a plasma to not be present, these inclusions can be ignored.

Before describing the particle pusher as it will be used for the single-particle model, a few notes must first be made. A subscript of n indicates the value for present time. Subscripts of $n + \frac{1}{2}$ and $n + 1$ indicate values at a half-timestep and a whole timestep in

the future, respectively. The subscript $n+\theta$ indicates a weighted average as shown in Eqn. (3.11). Mattei stated that θ must satisfy $0.5 \leq \theta \leq 1.0$ to prevent divergence. He chose to use $\theta = 0.6$ in his modeling so this model will also use that value.

$$X_{n+\theta} = \theta X_{n+1} + (1-\theta)X_n \tag{3.11}$$

The system of equations for the particle pusher is shown in Eqns. (3.12). The values of $\vec{E}_{n+\theta}$ and $\vec{B}_{n+\theta}$ are calculated at $\vec{x}_{n+\frac{1}{2}}$.

$$\begin{aligned}
\alpha &= -\frac{e\Delta t}{2m} \\
\vec{x}_{n+\frac{1}{2}} &= \vec{x}_n + \frac{\Delta t}{2}\vec{v}_n \\
\vec{v}^* &= \vec{v}_n + \alpha\vec{E}_{n+\theta} \\
\vec{v}_{n+\frac{1}{2}} &= \frac{\vec{v}^* + \alpha[\vec{v}^* \times \vec{B}_{n+\theta} + \alpha(\vec{v}^* \cdot \vec{B}_{n+\theta})\vec{B}_{n+\theta}]}{1 + (\alpha B_{n+\theta})^2} \\
\vec{x}_{n+1} &= \vec{x}_n + \Delta t\vec{v}_{n+\frac{1}{2}} \\
\vec{v}_{n+1} &= 2\vec{v}_{n+\frac{1}{2}} - \vec{v}_n
\end{aligned} \tag{3.12}$$

After the the system of equations is evaluated, the processes for wall reflections and Method 2 collisions are conducted as previously stated. However, Method 1 collisionality requires a small modification to Eqns. (3.12). To account for collision dampening, the term $\vec{v}_{n+\frac{1}{2}}$ is multiplied by the collision term in Eqn. (3.5) to get Eqn. (3.13).

$$\vec{v}_{n+\frac{1}{2}} = (1 - n_n\sigma v_{n+\frac{1}{2}})\vec{v}_{n+\frac{1}{2}} \tag{3.13}$$

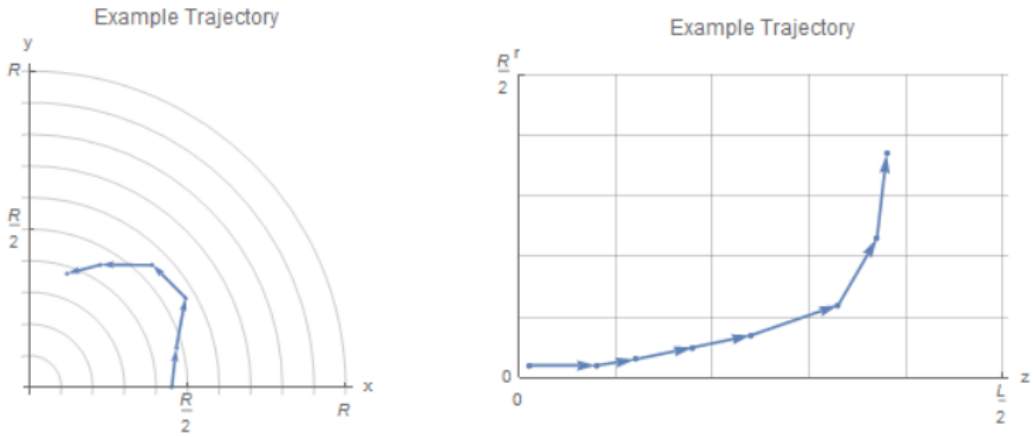

Figure 3.3. Example trajectory of particle overlaid on the field grid.

3.4. MODEL

The model starts the electron at a location on the x-axis, specifically $(\frac{R}{2}, 0)$, with no initial velocity. Eqns. (3.12) are used to move the electron. As the model accounts for the gyroperiod of an electron, the limiting term on the timestep is the collision rate. The collision period is $\tau = \frac{1}{n_n \sigma v}$. Mattei stated that for his particle pusher, the timestep must conform to $\Delta t < \frac{\tau}{100}$ and the minimum cell size must be such that particles cross no more than one cell boundary during a single timestep [38]. An example of a cell arrangement that conforms to Mattei's requirement is shown in Figure 3.3. Most ionization energies are on the scale of tens of eV. Thus, for a kinetic energy of 100 eV, a pressure of 50 mTorr, and a temperature of 300 K, the collision period comes out to be 1.05 ns. For $\Delta t < \frac{\tau}{100}$, the timestep will be chosen as $\Delta t = 10^{-11} s$. The associated minimum cell dimension for a kinetic energy of 100 eV is 0.06 mm. This model will use a minimum cell dimension of 0.1 mm or R/100, whichever is larger.

4. TOWNSEND BREAKDOWN MODEL

As discussed in Section 1.1.1, the Townsend Breakdown model is the most successful and most developed method for describing plasma formation. While it was intended only to describe a plasma in a DC electric field, attempts have been made to adapt it to other arrangements. The most relevant of these adaptations for the purposes of this work is the work done by Burm [13]. Burm equated the breakdown path of an ICP to the path in a parallel plate geometry folded in on itself. An example of this arrangement is shown in Figure 4.1. Part (a) of the figure shows a standard DC Townsend discharge where the breakdown path is bookended between two electrodes. Part (b) of the figure shows how, as a result of the path being curved, there is no defined start or end point for the discharge. Instead, the discharge feeds back in on itself. This layout led Burm to make two key changes to the Townsend Breakdown model so as to apply it to ICPs. First, as there is no electrode that feeds the discharge, secondary electrons will not provide a significant effect. Thus, β in Eqn. (1.2) is dropped. Second, as the discharge feeds back in on itself, there is no set length for the discharge path as opposed to Eqn. (1.2) having a set length d. Burm nominally sets the path length to be the circumference of the solenoid at half its radius but their derivations suggest it could be extended to any length.

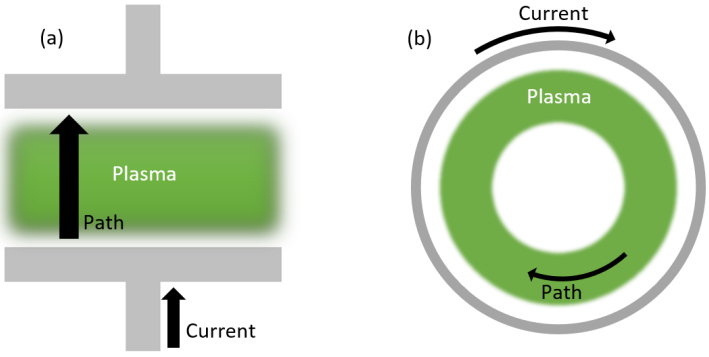

Figure 4.1. Breakdown path for (a) a DC Townsend discharge and (b) an ICP.

As previously discussed, the goal of Burm's model was to develop Paschen curves relating the possibility of breakdown to the magnetic field and the gas pressure. This effort was made possible because the magnetic field in an ICP is coupled to the electric field by way of Faraday's Law. In doing so, however, Burm chose to ignore any time-varying aspects of the plasma by using the magnitudes of the magnetic and electric fields. This work will modify Burm's approach by using the position- and time-dependence of the fields and then solve for the plasma number density as a function of time.

4.1. TOWNSEND BREAKDOWN IN AN INDUCTIVELY-COUPLED PLASMA

The Townsend Breakdown model describes the electric current between two parallel plate electrodes as Eqn. (1.2). The two critical terms are the first Townsend ionization coefficient, α, and the second Townsend ionization coefficient, β. The first coefficient describes free electron formation due to ionizing collisions and the second coefficient describes free electron formation due to emission from the cathode. The initial equation as shown in Eqn. (1.2) is typically modified by replacing β with the term $\gamma = \frac{\beta}{\alpha}$. This modified equation is shown in Eqn. (4.1).

$$\frac{I}{I_o} = \frac{e^{\alpha d}}{1 - \gamma(e^{\alpha d} - 1)} \tag{4.1}$$

However, as previously stated, β can be dropped as there are no electrodes affecting the ICP. From Burm's work, a differential term describing electron formation in such a system is given as Eqn. (4.2) [13].

$$dS = \alpha n_o e^{\alpha \Delta x} dx \tag{4.2}$$

If the electron is assumed to travel along a circular arc of length l parallel to the electric field, as shown in Figure 4.1, such that the field remains constant then Eqn. (4.2) can be integrated to give Eqn. (4.3). The electron's velocity is given as v and the arc length is given as $l = v\Delta t$.

$$\Delta S = n_o(e^{\alpha v \Delta t} - 1) \tag{4.3}$$

The first coefficient, α, was defined by Cobine as Eqn. (4.4) [2]. Note the dependence on the electric field, E, and the gas pressure, P. The values of C_a and C_b were defined in Table 7.1 of the text for a few different gases.

$$\alpha = C_a P e^{-\frac{C_b P}{E}} \tag{4.4}$$

More recent work has shown that the first coefficient changes when a magnetic field is applied to the region in question. Sen wrote that the presence of a crossed magnetic field can best be represented as a change to the pressure term in Eqn. (4.4) [7]. Specifically, he replaced the true pressure term with an effective pressure as given in Eqn. (4.5). H is the magnetic field in a medium and can be effectively equated to B in a low-pressure gas. C_c is a constant as given in Eqn. (4.6). Λ is the mean free path of the electron at 1 mmHg. u is the electron velocity.

$$p_e = p\sqrt{1 + C_c(\frac{H}{p})^2} \tag{4.5}$$

$$C_c = (\frac{e\Lambda}{m_e u})^2 \tag{4.6}$$

Radmilovic-Radjenovic provided an updated version of Eqn. 4.4 [9]. This version is given in Eqn. 4.7. The term κ is stated to be an empirical term equal to 1 for molecular gases and 2 for atomic gases. Values of A_κ and B_κ were provided for argon and nitrogen. However, as these values are not much different from the values given by Cobine [2], this model will use his original values, especially as they are provided for a wider range of gases. In the event that this model is applied to a wider range of gases, analytical equations for A_κ and B_κ developed by Burm [39] will be used.

$$(\frac{\alpha}{p_e})_E = A_\kappa e^{-B_\kappa(\frac{p_e}{E})^{\frac{1}{\kappa}}} \tag{4.7}$$

A series of plots showing how the addition of a magnetic field affects the First Ionization Coefficient is depicted in Figure 4.2. The magnetic fields in question are shown in Figure 4.3. As the plots show, the presence of a magnetic field constrains the 1st coefficient to be effectively nonzero only when the magnetic field is near zero. Thus, providing a bias field changes when the First coefficient peaks. In practice, the velocity will be coupled to the electric and magnetic fields. However, arbitrary values are used for this figure to show how it affects the final results. As shown, it only provides an asymptotic nature in that it increases the height of the peak up to the original non-B value and then proceeds to widen the peak once it has reached that limit. In practical terms, these modifications to the system will be manifested as a plasma only forming when the magnetic field is near zero. Furthermore, plasma formation is made more difficult when a bias magnetic field is applied.

4.2. CONTINUITY EQUATION

Unlike the Single-Particle Model where it assumed additional free electrons are only produced when the particle's energy crosses the ionization threshold, the Townsend-Breakdown model assumes that free electrons are being produced continuously. Past work

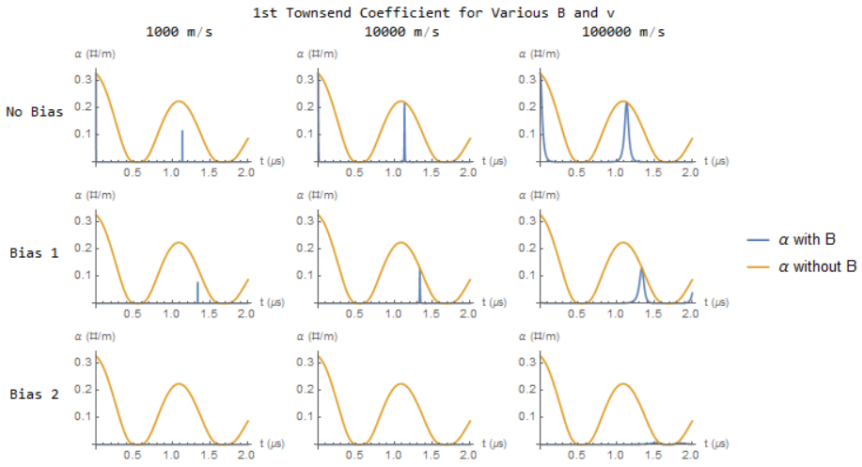

Figure 4.2. Townsend 1st ionization coefficient in a magnetic field.

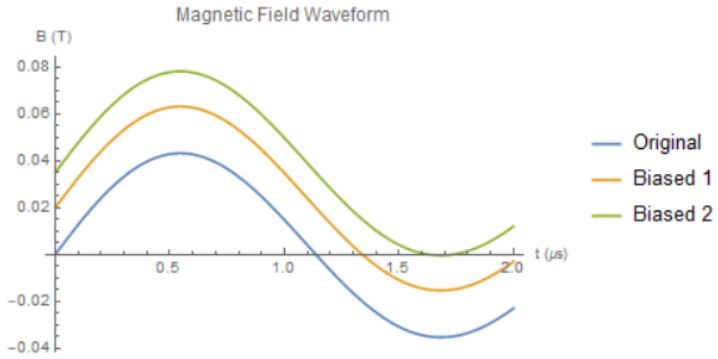

Figure 4.3. Magnetic Fields for Figure 4.2.

with Townsend breakdown has equated plasma formation to when the creation rate equals or is greater than the loss rate of charged particles. Thus, the governing equation for such a system is the continuity equation for free electrons as given in Eqn. (4.8).

$$\partial_t n + \nabla \cdot (Dn) = S(t) - L(t) \tag{4.8}$$

The first term, $\partial_t n$ is the time rate of change of the number density, n. The second term, $\nabla \cdot (Dn)$, describes the net motion of particles out of the system. D is the diffusion coefficient. The third term, $S(t)$, is the creation rate and the final term, $L(t)$, is the loss rate. The loss

rate specifically describes the loss of electrons due to recombination with ions. Therefore, because the number density of electrons and ions is negligible before a plasma forms, the loss rate will be treated as effectively zero for the application of this model.

For a small enough time step, the velocity of a particle can be assumed as effectively constant such that $\Delta x \approx v\Delta t$. Thus, Eqn. (4.2) can be rewritten as Eqn. (4.9). Note that n_o is changed to n to reflect the change from a constant to variable.

$$S(t)dt = \alpha n v e^{\alpha v \Delta t} dt \tag{4.9}$$

The velocity, v, is the velocity parallel to the electric field. In the case of an azimuthal electric field, the component of the velocity that would then affect ionization is the azimuthal component.

The final term that needs description in Eqn. (4.8) is $\nabla \cdot (Dn)$, the term that describes net motion out of the system. Rather than attempt to calculate D directly, it is more prudent to quantify the individual mechanisms that contribute to it. There are two such mechanisms that affect the net motion out of a system: diffusion and electromagnetic drift.

In the absence of a pressure gradient, the fastest a particle can be expected to move on behalf of pressure diffusion is the speed of sound. For argon at a standard operating temperature of 300 K, the speed of sound is 274 m/s. Over a period of, say, 2 μs, that translates to a maximum possible displacement due to pressure diffusion of 0.55 mm. This distance is not liable to change significantly for other gases given as the speed of sound is proportional to the square root of gas properties. Ultimately, unless the device in question has a characteristic length of a few mm or there exists a pressure gradient capable of driving particle speed past the speed of sound, diffusion due to pressure can be safely ignored.

As pressure diffusion is too weak to significantly affect a plasma on the time scales that will be used for this model, electromagnetic drift will be used as the primary loss mechanism. Recall the momentum equation presented in Eqn. (3.1). If collisions are ignored and the electric and magnetic fields are assumed to be strictly azimuthal and axial, respectively, the equations given in Eqns. (4.10) arise.

$$\begin{aligned} \partial_t v_r &= -\frac{e}{m} v_\phi B \\ \partial_t v_\phi &= -\frac{e}{m}(E - v_r B) \\ \partial_t v_z &= 0 \end{aligned} \tag{4.10}$$

Recall that the ionizing velocity was previously assumed to be approximately constant. If that assumption is maintained such that $\partial_t v_\phi \approx 0$, Eqns. (4.11) and (4.12) are the result.

$$\begin{aligned} \partial_t v_\phi &\approx 0 \\ E &\approx v_r B \\ v_r &\approx \frac{E}{B} \end{aligned} \tag{4.11}$$

$$\begin{aligned} \partial_t\left(\frac{E}{B}\right) &\approx -\frac{e}{m} v_\phi B \\ v_\phi &\approx -\frac{m}{e}\frac{E'B - EB'}{B^3} \end{aligned} \tag{4.12}$$

Note that the radial velocity comes out to the standard form of the $E \times B$ velocity. The two approximations, Eqns. (4.11) and (4.12), are particularly useful as analytic values for the electric and magnetic fields are not attainable. However, recalling Eqns. (2.22) and (2.23), analytic equations are available for the time-dependent components of the fields so the time-derivatives will be easy to perform.

To calculate the number density, the region in question will first be broken up into individual volume elements. As the system exhibits radial symmetry, the volume elements will be rings with rectangular cross-sections. An example of one of these cross-sections is

shown in Figure 4.4. Each ring cross-section will contain three locations at which the fields are calculated: the inner edge, the outer edge, and the halfway point. At the two edges, the fields will be used to calculate the radial velocity, v_r, via Eqn. (4.11). At the halfway point, the fields will be used to calculate the magnitude of the azimuthal velocity, v_ϕ via Eqn. (4.12). Thus, the net drift will be calculated as Eqn. (4.13). The terms N_1 and N_3 are the number of particles crossing the boundaries. They can be determined by setting $N_{i,3} = N_{i+1,1}$ and using the macroscopic boundary conditions $N_{1,1} = 0$ and $N_{i_{max},3} = 0$ to indicate no drift across the center axis of the cylinder or across the outer wall. These macroscopic boundary conditions are shown in Figure 4.5. Note that as the length of the cylinder is not included in any of the calculations, the terms N_1 and N_3 are implicitly scaled with length and thus are not true particle numbers.

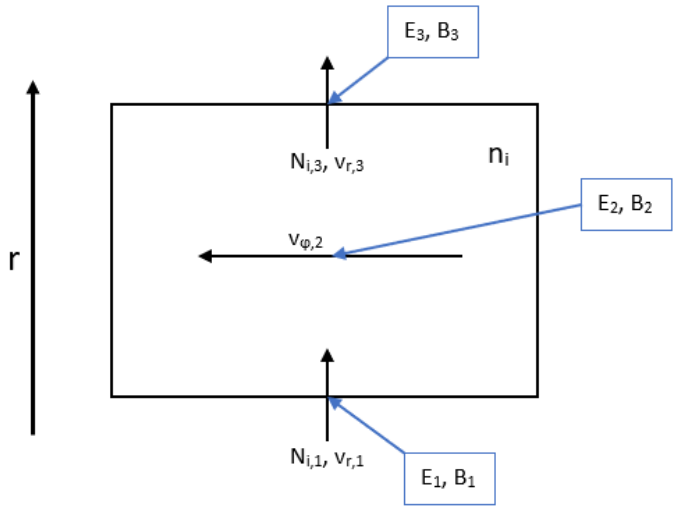

Figure 4.4. Individual cell for Townsend Breakdown model.

$$\nabla \cdot (Dn) = \frac{N_3 v_{r,3} - N_1 v_{r,1}}{2\pi r \Delta r} \tag{4.13}$$

Having developed terms for net particle potion and the creation rate, the continuity equation in Eqn. (4.8) can be restated as Eqn. (4.14) where the differentials are approximated as differences. This equation is solved for every volume element in the system.

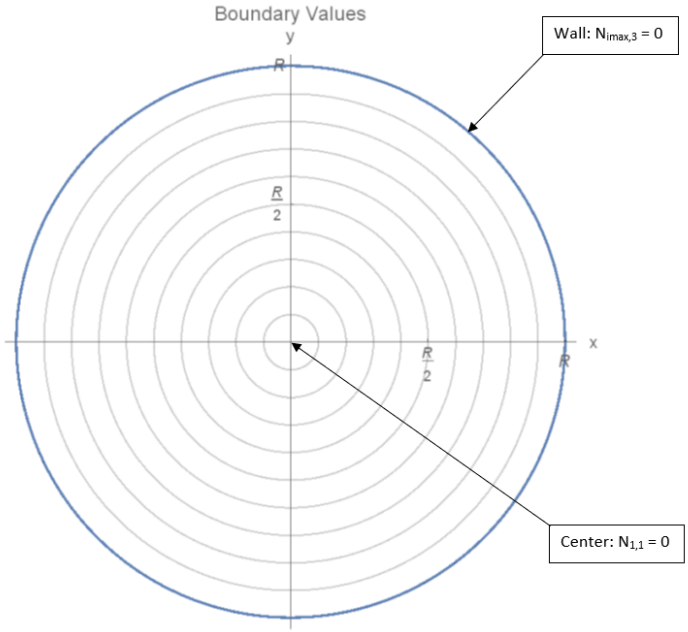

Figure 4.5. Boundary values for Townsend Breakdown model. $N_{max,3} = 0$ means that no particles drift across the wall. In other words, the wall is reflective, not absorbing. $N_{1,1} = 0$ means that the innermost cell loses no particles to drift across the axis. Due to the shape of the innermost cell, any particle that drifts across the axis will not exit the cell.

$$\Delta n = \alpha n v_{\phi,2} e^{\alpha v_{\phi,2} \Delta t} \Delta t + \frac{N_1 v_{r,1} - N_3 v_{r,3}}{2\pi r \Delta r} \Delta t \tag{4.14}$$

The value of n used in Eqn. (4.14) is the number density calculated for the previous time step, n_{j-1}. Having evaluated for Δn, the new value of the number density is calculated using the following equation.

$$n_j = n_{j-1} + \Delta n$$

As gyromotion of individual electrons is not modeled in this approach, this model is free to use a larger, and thus less resource intensive, value for Δt than was available for the Single-Particle Model.

5. MPX ANALYSIS

The MPX, or Missouri Plasmoid Experiment, is a testbed designed by Pahl at the Missouri University of Science and Technology to study pulsed-inductive FRC plasmas [40]. Two versions were made, the MkI shown in Figure 5.1 and the MkII shown in Figure 5.2. The MkI is a copper sheet rolled to an inner radius of 8.9 cm and an axial length of 76.2 cm. The MkII is a series of 11 aluminum blocks with a circular channel carved through them bearing an inner radius of also 8.9 cm. In both designs, the plasma is formed inside a quartz tube with an inner radius of 7.725 cm. Due to the rolling process used to shape it, the MkI does not possess a perfectly circular cross-section. This abnormality has led to small perturbations in the electromagnetic fields and thus an unstable plasma. The MkI has an inductance of 37.2 nH and the MkII has an inductance of 36.2 nH. As the external circuit is the same for both designs, the current waveform is very nearly the same. The results that will be discussed in this section are for the MkI as it, not the MkII, was used by Meeks for breakdown studies [41]. One result from the MkII that will be considered is pressure distribution. Pahl found that a plasma would consistently form for pressures between 20 mTorr and 100 mTorr [42]. Between 0 mTorr and 20 mTorr, he found that a plasma could still form but was inconsistent in doing so. It was only after treating the gas with a glow discharge first that he could reliably obtain breakdown in that pressure range [43].

In this chapter, particulars of the geometry of the MkI will be discussed first. After that, a comparison will be made between the fields calculated using the equations specified in Section 2 and the theoretical values for a cylinder. Finally, the results for the individual models will be presented and then discussed.

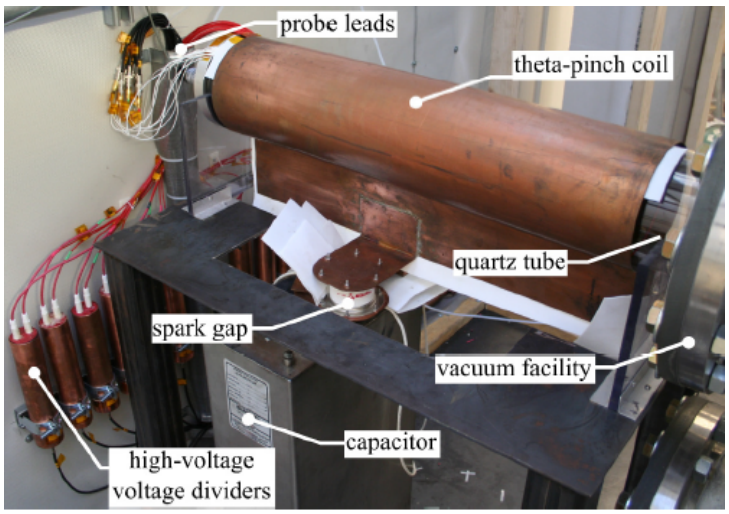

Figure 5.1. Image of the MPX MkI with notations.[40]

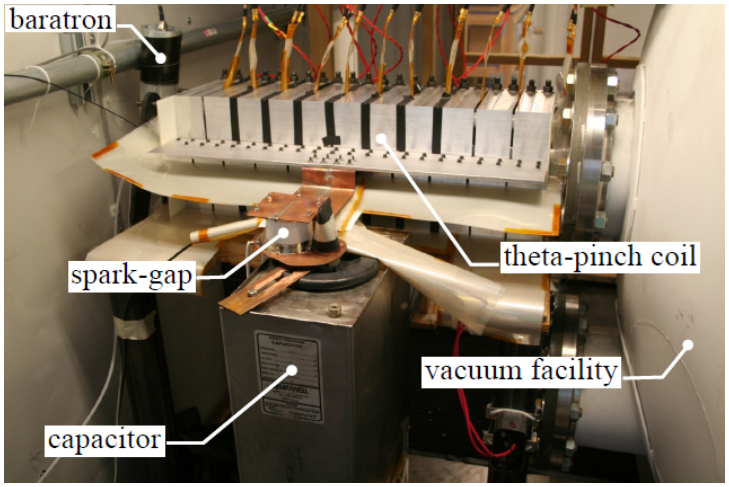

Figure 5.2. Image of the MPX MkII with notations.[40]

5.1. GEOMETRY

The MPX MkI is a rolled copper sheet with an inner radius of 8.9 cm and a length of 76.2 cm [40]. The electric current in the copper sheet and the measured plasma potential are both shown in Figure 5.3. The blue curve is the electric current and the green curve is the measured plasma potential. The equation for the current is given in Eqn. (5.1) where t is in units of s and I is in units of A. According to Meeks, the time at which the plasma

potential begins to oscillate, approximately 1.14 μs, is the time at which a plasma has officially formed inside the system. An image of the plasma produced by the MPX MkII, Figure 5.4, shows that the density is highest near the walls of the chamber. The two designs were previously shown to be near identical in operation so it will be inferred that the peak plasma density in the MkI must also be highest near the chamber walls. The chamber is a quartz tube with an inner radius of 7.725 cm and a length of 9.15 cm. The gas from which the plasma forms is Argon. A listing of the properties that will be used for the modeling is shown in Table 5.1.

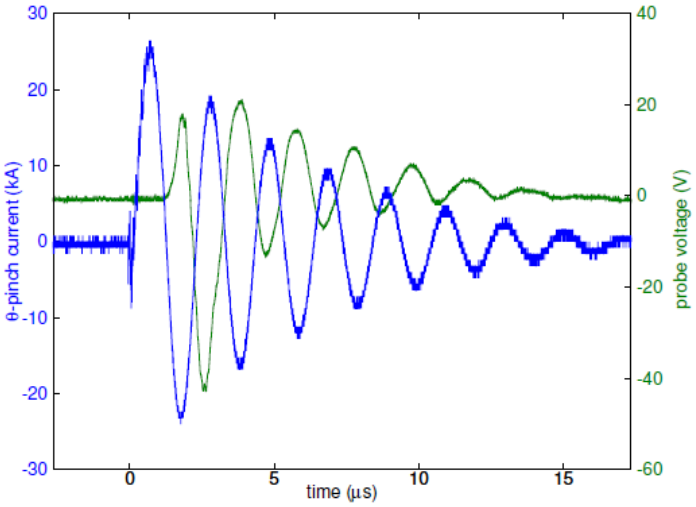

Figure 5.3. Applied current and measured plasma voltage of the MPX MkI.[41]

$$I(t) = 28880e^{-175107t}\sin(2\pi 440000t) \tag{5.1}$$

Table 5.1. Properties for modeling MPX MkI.

Chamber Properties		**Gas Properties**	
Coil Radius (cm)	8.9	Gas	Argon
Coil Length (cm)	76.2	E_{ion} (eV)	15.76
Chamber Material	214 Quartz	σ (m^2)	1×10^{-19}
Chamber Radius (cm)	7.725	C_a ($\frac{1}{m \cdot Pa}$)	10.2
Chamber Length (cm)	91.5	C_b ($\frac{V}{m \cdot Pa}$)	176.25
		T (K)	300

Figure 5.4. Plasma formation in the MPX MkII. [40]

5.2. FIELD COMPARISON

Before running the individual models, the calculated values of the electric and magnetic fields will first be compared to the theoretical values for a cylindrical solenoid. The theoretical values are chosen instead of experimental values because Pahl chose to use the theoretical values as his baseline [42]. The theoretical values are obtained from equations for an infinite solenoid and are shown in Eqns. (5.2) and (5.3). For a single-turn solenoid, $N = 1$. Note that the magnetic field does not vary with position.

$$B = \frac{\mu_o N I}{L} \tag{5.2}$$

$$E = -\frac{r}{2}\partial_t B \tag{5.3}$$

Comparisons of the theory and the numerically integrated magnetic field are shown in Figures 5.5 and 5.6 along with the difference. Comparisons of the theory and the calculated electric fields are shown in Figure 5.7. Note that every comparison for both the magnetic and electric fields shows the calculated value to be slightly smaller than the theory. The reason for this discrepancy is likely due to the finite size of the MPX. While Eqn. (5.2) does account for the finite length of a solenoid, it assumes that the magnetic field is perfectly uniform inside the solenoid, regardless of distance from the axis. In reality, a minimal radial gradient is to be expected. It is fair to say then that the calculated values of the fields do not significantly diverge from the theory.

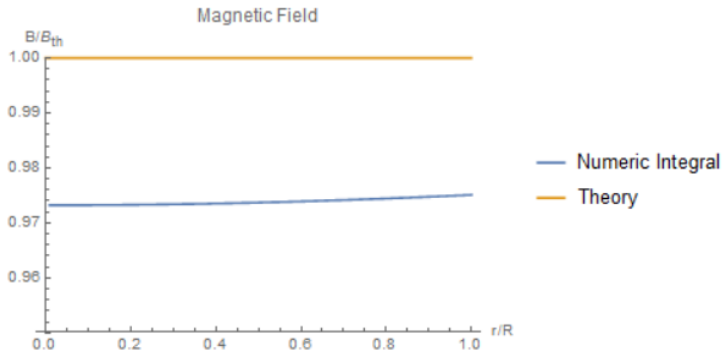

Figure 5.5. Comparison of magnetic field due to ideal solenoid theory and field due to 3D numeric integrals at 1 μs after start. The radii are normalized with respect to the coil radius. The fields are normalized with respect to the theory.

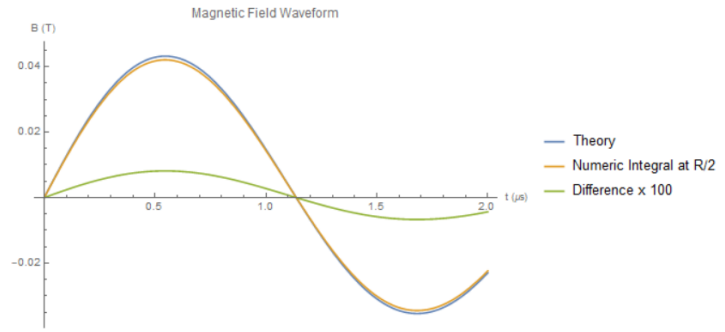

Figure 5.6. Comparison of magnetic field due to ideal solenoid theory and field due to 3D numeric integrals at half-radius. The difference between the two fields is shown and has been multiplied by 100 for clarity.

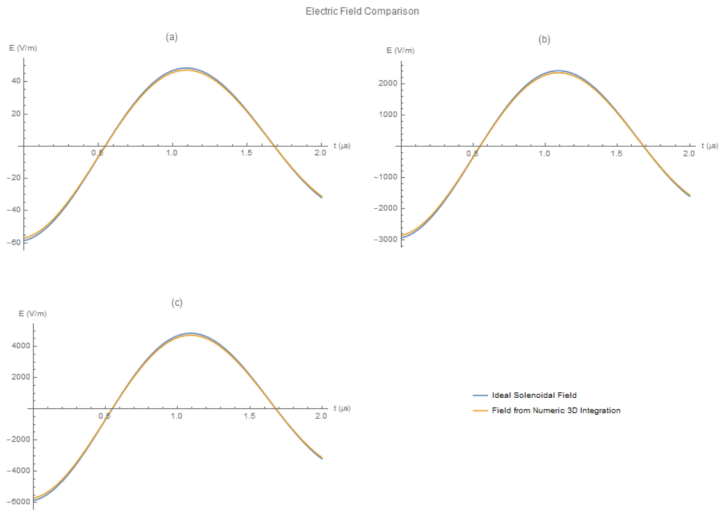

Figure 5.7. Comparison of electric field due to ideal solenoid theory and field due to 3D numeric integrals (a) near the axis, (b) at the half-radius, and (c) near the wall.

5.3. RESULTS

Results for the Single-Particle Model are given in Section 5.3.1 with test parameters given in Table 5.2. Results for the Townsend-Breakdown Model are given in Section 5.3.2.

Table 5.2. Single-Particle Model parameters for MPX MkI.

Simulation Properties	
Time Step (μs)	1×10^{-5}
Number of Time Steps	2×10^{5}
Time Range (μs)	2
Cell Size (Radial) (cm)	0.07725
Number of Cells (Radial)	100
Start Position (x) (cm)	4.5
Initial Speed (m/s)	0
Test Pressures (mTorr)	5, 10, 20, 30, 40, 50

5.3.1. Single-Particle Model. The initial values of the single-particle model (SPM) are zero velocity and a starting position at the half-radius, 4.5 cm from the center. The model was run for several pressures ranging from 5 mTorr to 50 mTorr. This range encloses the range of pressures in which the plasma is stated to form. As the active gas is Argon, the

ionization energy threshold was set to 15.76 eV. The time step was set to 0.5 fs and the range was set to 2 μs. Recall that two different approaches to modeling collisions were proposed in Section 3.1. Results for both methods will be presented. Dampening collisionality will be identified as Method 1 and particle collisionality will be identified as Method 2.

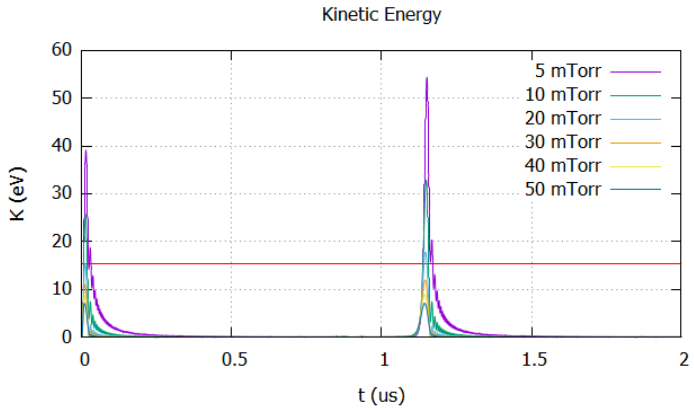

Figure 5.8. Single electron kinetic energy for Method 1. The horizontal line marks ionization energy for Argon.

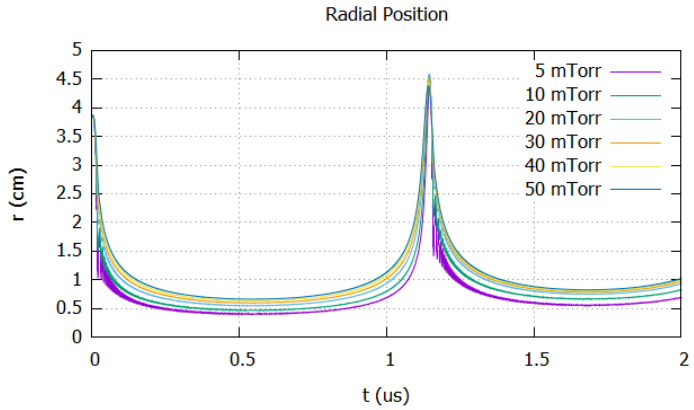

Figure 5.9. Single electron radial position for Method 1.

Results for pressures of 5, 10, 20, 30, 40, and 50 mTorr are shown in Figures 5.8 and 5.9 for Method 1 and Figures 5.10 and 5.11 for Method 2. The red horizontal line in the kinetic energy plots depicts the ionization energy threshold that must be met. The results for Method 1 show a strong energy spike at the start followed by a quick drop to

near zero within the first 0.1 μs. The results then show another strong energy spike at about 1.15 μs. A cutoff due to the threshold can be discerned between 20 and 30 mTorr where higher pressures fail to meet the threshold. This second spike occurs at the time when ionization is expected. In both cases, the radial plots show that the electron is at its max radial position when it reaches ionization energies. This result agrees with the experimental result where plasma is most intense near the walls of the system. Where the results for Method 1 present a simple pattern relating pressure to energy, the results for Method 2 are borderline incomprehensible. Some patterns can be gleaned from the data in Figure 5.10. One is that higher pressures take longer to gain energy at the start. Another is that all the pressures appear to spike at the same time at about 1.1 μs. This collective spike coincides with a maximum in the radius shown in Figure 5.11. However, no clear pattern is shown relating pressure to energy or radius at that time. This lack of a pattern is most evident in Figure 5.11 where the order of of maxima does not correspond to the pressures. Where the results for Method 1 have a clear correlation between high energies and high radial positions, the results for Method 2 do not. From a modeling standpoint, it is likely that the high energies at low radii are due to the electron is gyrating about the central axis of the cylinder where, due to the low pressure, it never travels a full mean free path from its previous collision spot and thus never triggers a new collision. From a physical standpoint, the lack of collisions would indicate that, even though the energy is high, no ionization occurs. To account for that physical phenomena, the code could output only the kinetic energies at times corresponding to collisions. Such a method could filter out the anomalous energies and present better agreement with the results of Method 1. However, it would not magically fix the lack of a pattern relating pressure to energy or radial positon.

5.3.2. Townsend-Breakdown Model. The time step was set to 0.2 ns and the range to 2 μs. As with the single-particle model, the Townsend-Breakdown model (TBM) was run for pressures ranging from 5 to 50 mTorr. However, no change in the results were found past 15 mTorr. Thus, results are only shown for 5, 10, and 15 mTorr. The initial number

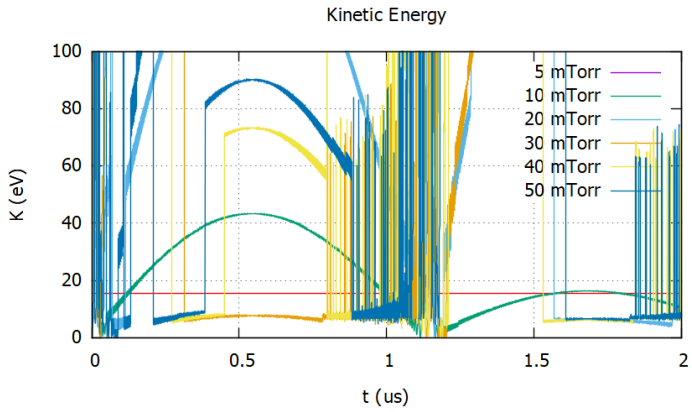

Figure 5.10. Single electron kinetic energy for Method 2. The horizontal line marks ionization energy for Argon.

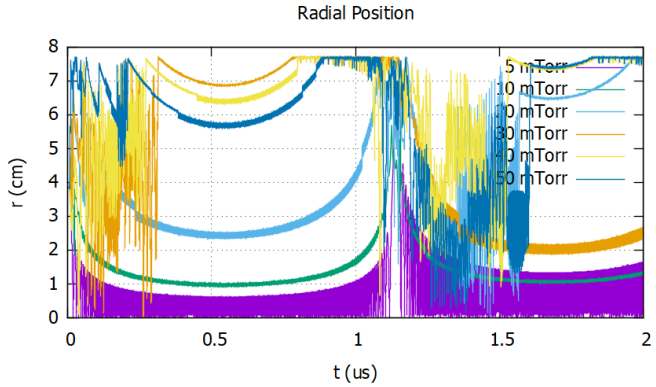

Figure 5.11. Single electron radial position for Method 2.

density was set to 10^{-1} cm^{-3}. The results are shown in Figures 5.12 and 5.13. The first set of plots shows the time-evolution of the number densities at several radial positions. The second set of plots shows the time-evolution of the creation rate at the same radial positions. For reference, the neutral number density at 5 mTorr and 300 K is 1.61×10^{14} cm^{-3}. Not only are the predicted number densities physically possible but the trends show agreement with the experimental results. The plots in Figure 5.13 show the rate of creation rather than a cumulative sum of particles created. Notice that a significant creation event occurs

at about 1.15 μs, the expected time of plasma formation, and is strongest at the outermost radial positions. The high densities at low radii are likely due to the electromagnetic drift as Figure 5.13 shows the creation rate at those positions staying low.

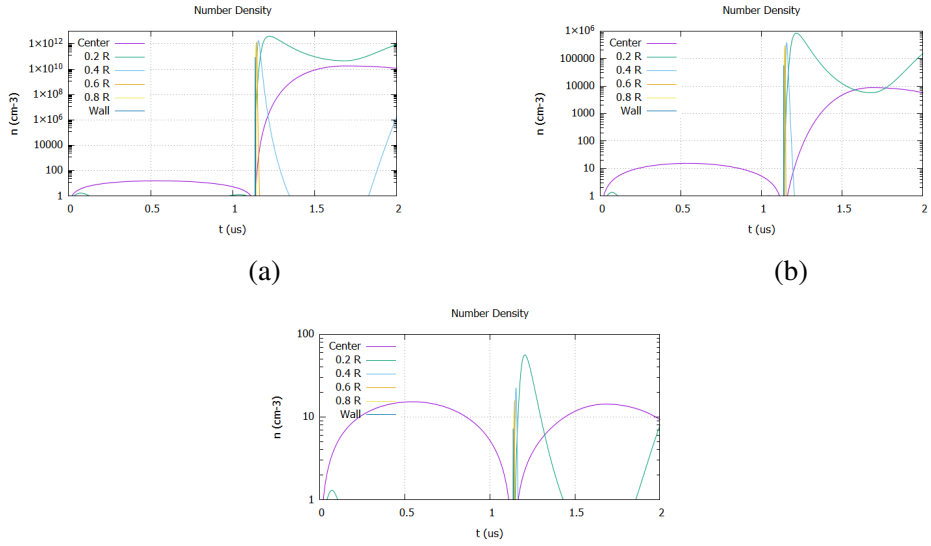

Figure 5.12. Electron number densities at (a) 5 mTorr, (b) 10 mTorr, and (c) 15 mTorr.

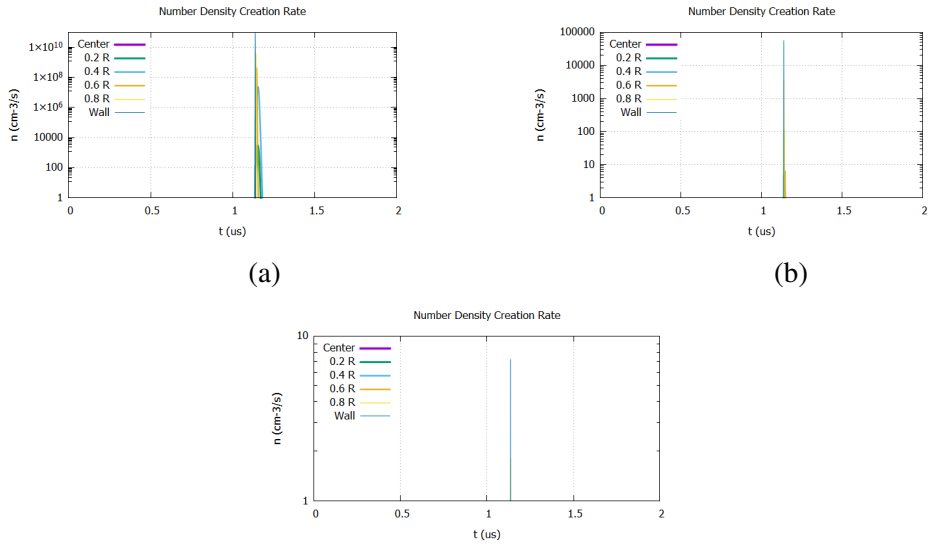

Figure 5.13. Electron creation rates at (a) 5 mTorr, (b) 10 mTorr, and (c) 15 mTorr.

5.4. ANALYSIS OF RESULTS

Neither model perfectly mimics the experimental results shown in Figures 5.3 and 5.4. Method 1 of the SPM and the TBM both show agreement with when and where plasma formation is expected to occur. However, Method 1 of the SPM also shows strong energy spikes at the beginning of the run time. In addition, both models show disagreement with the expected pressure range over which a plasma has been shown to form. The SPM predicts that the ionization threshold will not be met above 20 mTorr and the TBM shows effectively no plasma number density above 15 mTorr. Another obstacle to the legitimacy of these models is the confinement of charged particles to the inner radii. In both models, high energies and creation rates are achieved at high radii but these processes are not sustained as the electrons proceed to retreat to lower radii. There are two complementary options that can be considered to resolve this obstacle.

The first option is a physical result of the charged particle motion. In both the SPM and the TBM, the particles are cumulatively traveling in loops around the central axis of the cylinder. This motion generates what is effectively a current opposing the applied current. In practice, this opposing current would subsequently generate an opposing electric field to the original applied field. The resultant weakening of the electric field would diminish the electromagnetic drift that pulls charged particles back to the center of the cylinder and would also reduce the strength of the creation events in the TBM. Another way of looking at it is that the growing number of charged particles dampen further creation of charged particles. The absence of such dampening in the model as it currently stands could explain why unrealistically high values of the number density are currently being achieved. A plot showing the influence that electron number density has on the electric field is shown in Figure 5.14. As the figure shows, the electric field does not begin to noticeably perturb until the number density is higher than 10^{16} m^{-3} or 10^{10} cm^{-3}.

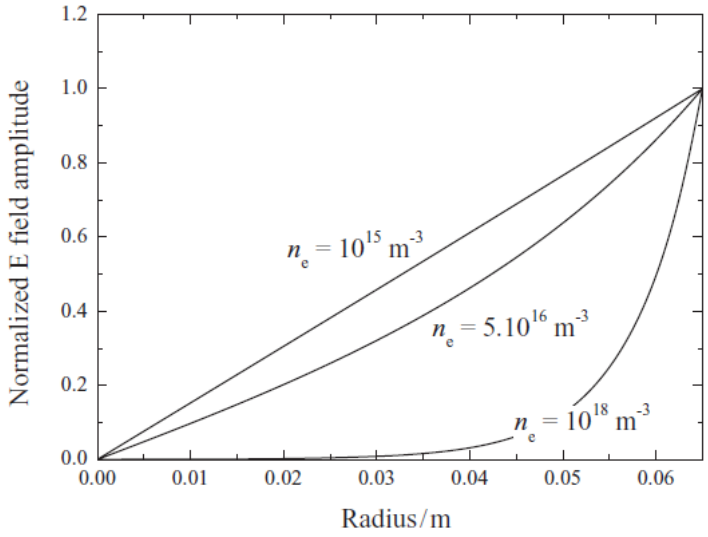

Figure 5.14. Electric field variance due to electron number density. [10]

The second option is to account for a capacitive electric field. Chabert and Braithwaite state that capacitive coupling in an inductively-coupled plasma is strongest at low electron densities and has been found to be essential to ignition of an ICP [10]. As the applied current changes with time, a potential difference across the device is introduced in accordance with Eqn. (5.4). Due to the geometry of the theta-pinch, a strong capacitive field will form at the lip where the device is folded to allow current to enter and exit. The capacitive field for the MPX is shown in Figure 5.15. As the figure shows, the capacitive field is not azimuthally symmetric nor is it negligible. In fact, the capacitive field is much stronger than the inductive field, shown in Figure 5.7, that is present along the wall of the cylinder.

$$V = L\partial_t I(t) \tag{5.4}$$

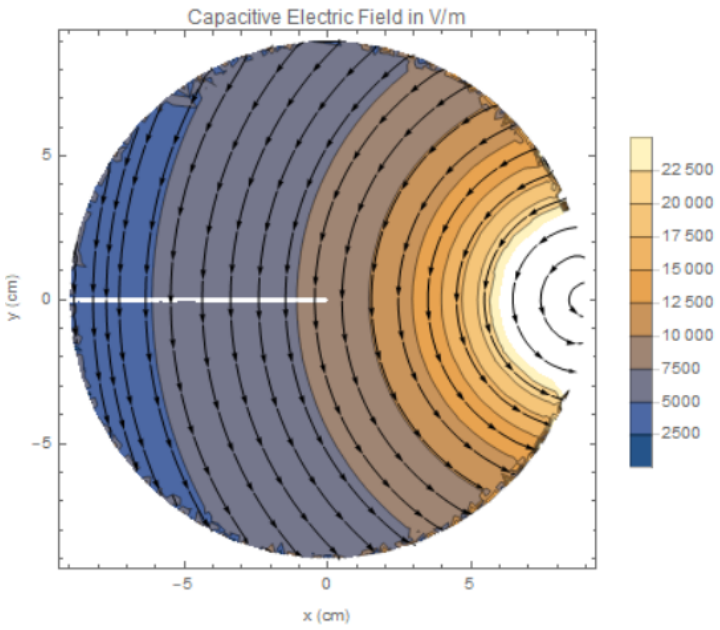

Figure 5.15. Capacitive electric field due to single-turn theta-pinch configuration at 1 μs after system start. The current enters and exits the theta-pinch at (9 cm, 0 cm).

6. FRCHX ANALYSIS

The Field Reversed Configuration Heating Experiment (FRCHX) is described by Grabowski [29] with breakdown studies conducted by Meeks [30]. A diagram of the device is shown in Figure 6.1. The FRCHX was designed to generate FRC plasmas for use in a variety of experiments. Unlike the MPX discussed in the previous section, the FRCHX begins the ionization process with a nonzero bias magnetic field. This bias field has the effect of shifting the phase of the magnetic field so that its zero values occur at the same time as the zero values of the electric field. As with the MPX, plasma formation was found to be delayed until the first zero values of the field. A plot of the magnetic field with annotations marking this delay is shown in Figure 6.2. In his breakdown study, Meeks suggested that the delay in breakdown could be attributed to the magnetic field confining electrons to small gyro-orbits [30].

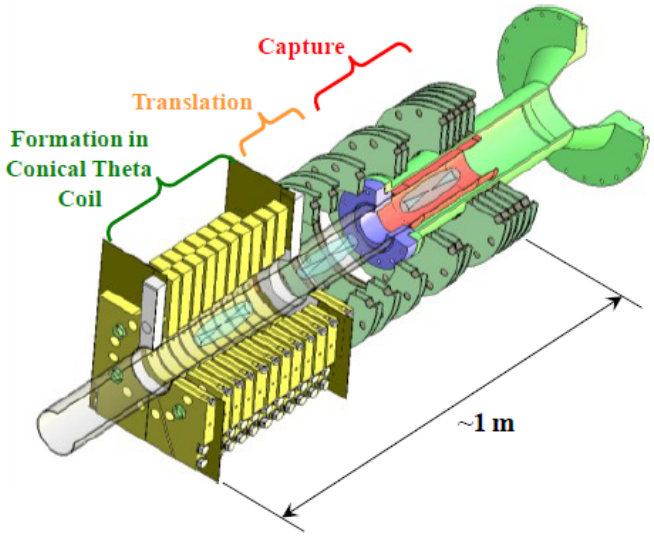

Figure 6.1. Diagram of the FRCHX. [29]

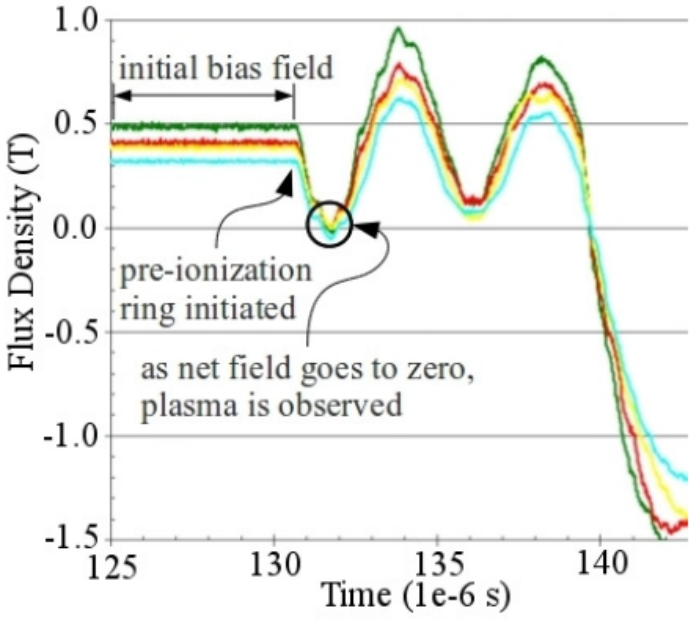

Figure 6.2. Magnetic Field Profile of FRCHX. [29]

6.1. GEOMETRY

From the diagram shown in Figure 6.1, it can be seen that the inductive coil for the preionization stage is conical instead of cylindrical. However, this attribute will be ignored for two reasons. First, the region in which the plasma itself forms is a cylinder with a radius of 6.5 cm. Second, only data for the axial component of the magnetic field is shown. As discussed in Section 5.1, it is standard for FRC plasmas to exhibit a max density near the walls. Thus, the expectation for the location of ionization in the models will be at or near the radius of 6.5 cm. In addition, as the radial component of the magnetic field is ignored, any motion along the axis will also be ignored as a radial magnetic field is the only means of electromagnetically driving electron motion along that direction in this system. Finally, the active gas in the FRCHX is Deuterium. Thus, the ionization energy threshold will be set to 15.47 eV. A listing of the properties that will be used for the modeling is shown in Table 6.1.

Table 6.1. Properties for modeling FRCHX.

Chamber Properties		**Gas Properties**	
Coil Radius (cm)	N/A	Gas	Deuterium
Coil Length (cm)	38	E_{ion} (eV)	15.47
Chamber Material	Quartz	σ (m^2)	7.85×10^{-21}
Chamber Radius (cm)	5	C_a ($\frac{1}{m \cdot Pa}$)	3.75
Chamber Length (cm)	45	C_b ($\frac{V}{m \cdot Pa}$)	97.5
		T (K)	300

6.2. FIELDS

As data for the magnetic field is already present as shown in Figure 6.2, the equations given in Section 2 will not be used. Instead, the magnetic and electric fields will be modeled according to equations used by Meeks [30]. The axial magnetic field is approximated as Eqn. (6.1) and the azimuthal electric field is approximated as Eqn. (6.2). The frequency f is 250 kHz. The term (T) indicates that the magnetic field is in units of Teslas. Using these equations, ionization will be expected to occur at 1 μs after start.

$$B(t) = -0.5 \sin(2\pi f t) + 0.5(T) \tag{6.1}$$

$$E(r,t) = -\frac{r}{2}\partial_t B(t) \tag{6.2}$$

6.3. RESULTS

Results for the Single-Particle Model are given in Section 6.3.1 with test parameters given in Table 6.2. Results for the Townsend-Breakdown Model are given in Section 6.3.2.

6.3.1. Single-Particle Model. The initial values of the single-particle model (SPM) are zero velocity and a starting position at the half-radius, 3.25 cm from the center. The model was run for several pressures ranging from 5 mTorr to 50 mTorr. This range encloses the range of pressures in which the plasma is stated to form. As previously mentioned,

Table 6.2. Single-Particle Model parameters for FRCHX.

Simulation Properties	
Time Step (μs)	1×10^{-7}
Number of Time Steps	2×10^{7}
Time Range (μs)	2
Cell Size (Radial) (cm)	0.065
Number of Cells (Radial)	100
Start Position (x) (cm)	3.25
Initial Speed (m/s)	0
Test Pressures (mTorr)	5, 10, 20, 30, 40, 50

the ionization energy threshold is set to 15.47 eV. Results for both methods discussed in Section 3.1 will be presented. As with the MPX, dampening collisionality will be identified as Method 1 and particle collisionality will be identified as Method 2.

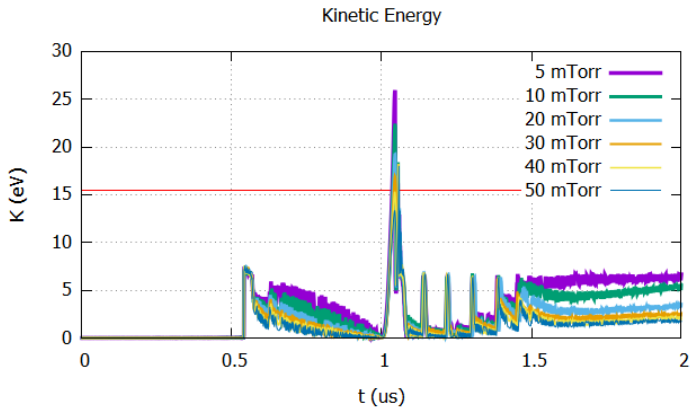

Figure 6.3. Single electron kinetic energy due to Method 1 of the SPM. The red horizontal line indicates the ionization threshold of 15.47 eV.

Results for pressures of 5, 10, 20, 30, 40, and 50 mTorr are shown in Figures 6.3 and 6.4 for Method 1 and Figures 6.6 and 6.7 for Method 2. In addition, a zoomed-in version of Figure 6.3 is shown in Figure 6.5. As with the MPX results, the red line in the kinetic energy plots corresponds to the ionization energy and the blue curve is the kinetic energy of the electron. Both sets of results show the energy spiking at about 0.55 μs. When compared to the radial plots, this spike can be seen to correspond to the electron getting pushed into

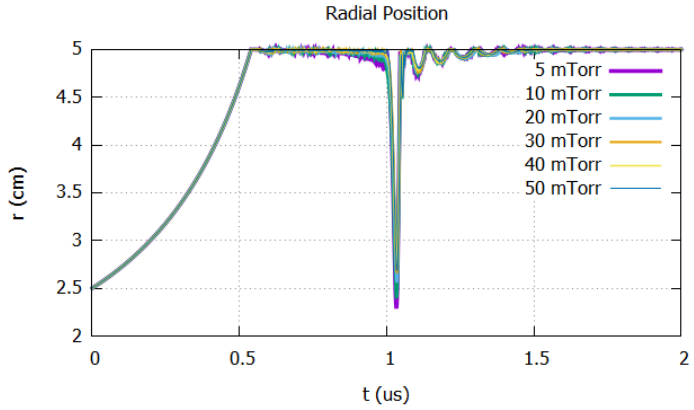

Figure 6.4. Single electron radial position due to Method 1 of the SPM.

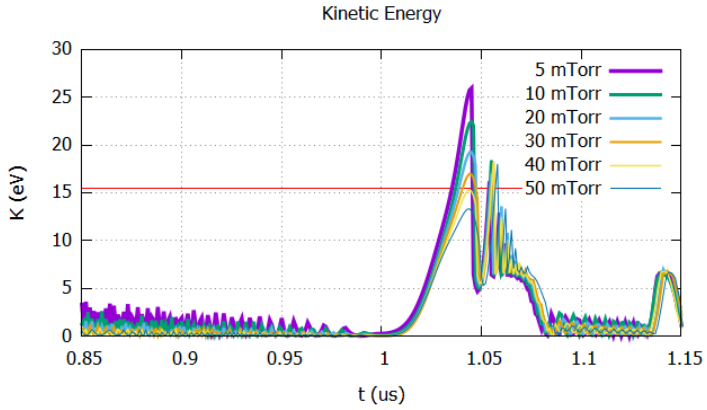

Figure 6.5. Single electron kinetic energy due to Method 1 of the SPM zoomed into a range of 0.85 to 1.15 μs. The red horizontal line indicates the ionization threshold of 15.47 eV.

the wall due to the fields. As the wall is modeled as quartz, the energy never surpasses 7 eV. Both plots show the energy gradually decaying back to zero but the decay is more pronounced in Figure 6.3 likely due to the dampening effects of Method 1 collisionality. In addition, both cases show an energy spike at about 1.04 μs. From comparison with the radial plots, this energy spike is shown to correspond to the electron moving inward away from the wall. This energy spike corresponds to when the experimental results show ionization to occur. Figure 6.5 shows that the cutoff for the ionization threshold is just shy

of 40 mTorr. No variation between pressures is shown in Figure 6.6 for Method 2 likely because the small collision cross-section of Deuterium means the electron is never able to travel a full mean free path-length for any of the pressures tested.

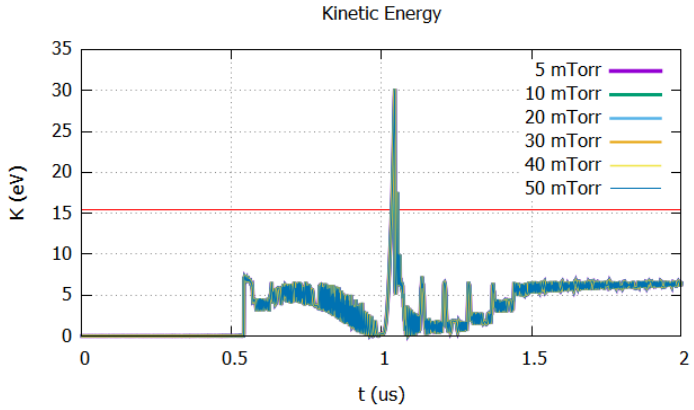

Figure 6.6. Single electron kinetic energy due to Method 2 of the SPM. The red horizontal line indicates the ionization threshold of 15.47 eV.

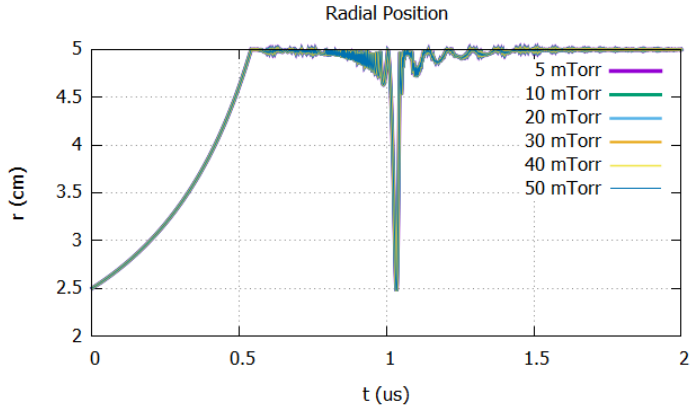

Figure 6.7. Single electron radial position due to Method 2 of the SPM.

6.3.2. Townsend-Breakdown Model. The time step was set to 0.2 ns and the range to 2 μs. As with the single-particle model, the Townsend-Breakdown model was run for pressures ranging from 5 to 50 mTorr. The results are shown in Figures 6.8 and 6.9. The plots in Figure 6.8 show the time-evolution of the number densities at several radial positions. The plots in Figure 6.9 show the time-evolution of the creation rate at the

same radial positions. For reference, the neutral number density at 5 mTorr and 300 K is 1.61×10^{14} cm^{-3}. In every case, the number density is so small as to be negligible. However, the radial positions are an interesting divergence from the MPX results. As expected, a strong creation event occurs at 1 μs but the highest densities are shown to occur at the innermost positions despite the highest creation rates occurring at the outermost positions.

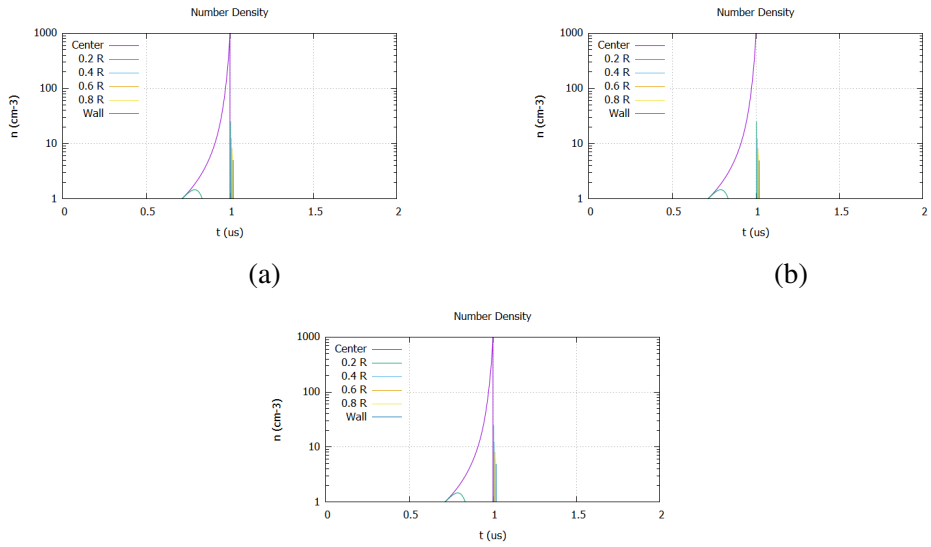

Figure 6.8. Electron number densities at (a) 5 mTorr, (b) 10 mTorr, and (c) 15 mTorr.

6.4. ANALYSIS OF RESULTS

Both methods for the Single-Particle Model show a notable spike in the energy at 0.55 μs. Comparing this time with the radial plots shows that in both methods, the electron is getting trapped at the wall. However, because the wall is modeled as being lossy, this spike is capped at just under 7 eV. Without the energy cap, it is fair to suggest the sudden energy rise would extend much further. This attribute where the wall serves as a repository for mid-level electrons may suggest that a particular type of boundary is essential to ICP formation in a theta-pinch.

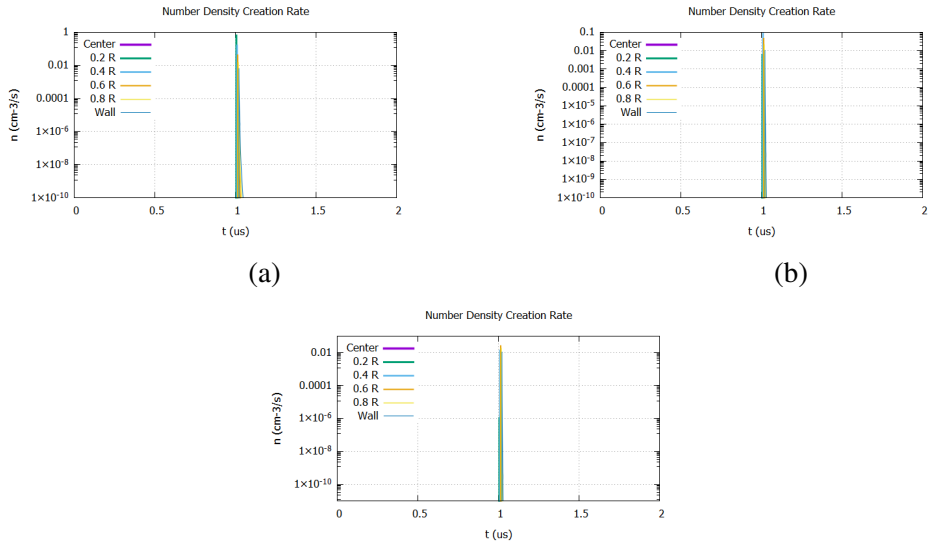

Figure 6.9. Electron creation rates at (a) 5 mTorr, (b) 10 mTorr, and (c) 15 mTorr.

It should be noted that the single-particle model employed by Meeks covered only a small period of the period [30]. Where the model presented here ran from 0 to 2 μs, Meeks ran his code from 0.85 to 1.1 μs with the electron having zero kinetic energy at 0.85 μs. His results, as do the results shown in Figure 6.5, depict ionization happening soon after 1.0 μs. Some justification is warranted for starting at the later time as the electron is shown to have less than 5 eV of energy at 0.85 μs.

The TBM predicts ionization as occurring at the expected time. However, unlike the results for the MPX, the number densities are too small for ionization to be reasonably possible. Recall the trend shown in Figure 4.2. When the magnetic field is offset such that it only tangentially reaches zero, the First Townsend Ionization Coefficient is effectively reduced to zero all the time. Thus, the number densities shown in Figure 6.8 are to be expected from a modeling standpoint as the magnetic field is set up in the same manner for the FRCHX. In further contrast to the MPX, while the creation rate appears to be highest at the outermost radii, the highest number density overall is at the lowest radius. This result is

likely due to the offset of the magnetic field changing which direction the fields cause the electrons to drift. This same inward drift is also present in the results for the SPM but only in the quarter-cycle after the creation event. This offset also causes both the magnetic field and the electric field to reach zero at the same time thus leaving the radial drift velocity with a zero divided by zero error that causes it to behave discontinuously. This discontinuous behavior could explain why the curve for the density of the lowest radius is disjointed at 1 μs.

An interesting comparison to be made between the results for the MPX and the FRCHX is the magnitude of the electron energy. The MPX puts the threshold between 20 and 30 mTorr where the FRCHX puts the threshold just under 40 mTorr. However, the energy at the lowest pressure tested, 5 mTorr, peaks at about 55 eV for the MPX while the corresponding peak for the FRCHX is about 26 eV, approximately half. At first, this reduced energy is odd. The max radial values are similar in both cases, 4.5 cm for the MPX and 5 cm for the FRCHX. The time-varying component of the magnetic field has a peak more than ten times stronger in the FRCHX than in the MPX, 0.5 T versus 0.04 T. Due to the relationship between the fields, this relationship carries over to the electric field. Finally, the frequency of the current waveform in the MPX is just under twice the frequency for the FRCHX, 440 kHz versus 250 kHz. All told, the maximum electric field experienced by the electron in the FRCHX should be about 7.9 times larger than the field in the MPX. Yet, the electron in the MPX is modeled as experiencing higher energies. This comparison makes some sense when Figure 4.2 is considered. The figure showed that ionization was harder to achieve when the magnetic field was offset by some value. That result agrees with the result shown here where, even though the FRCHX should be adding more energy to its system, the simulation of the MPX experiences higher maxima.

7. CTP-FARAD ANALYSIS

The FARAD, or Faraday Acceleration with Radio-frequency Assisted Discharge, was a planar device similar in design to the Pulsed-Inductive Thruster (PIT). It was designed by Choueiri to reduce the power needed to provide thrust by combining the planar coil from the PIT with a pre-ionization section [44]. A modification to Choueiri's design was proposed by Hallock in which a theta-pinch in the shape of a frustum is appended to the outlet from the FARAD [33]. The intent of the conical design is to align the magnetic field lines and the surface of the inductor with the natural flow of the propellant. Unlike the previously discussed MPX and FRCHX, the CTP-FARAD (Conical Theta Pinch - FARAD) functioned purely as an acceleration coil. Two different pre-ionization methods were used: a helicon coil as used in the original FARAD design [33] and an electrode spark [45]. An example of the former is shown in Figure 7.1. A modification to the CTP-FARAD was proposed by Feldman that would have converted the acceleration coil to a pre-ionization coil [46]. However, the only work that he produced on that front was a circuit analysis of the required changes. No experimental work was undertaken on developing the proposed design. Nevertheless, the results described for the initial acceleration coil are interesting and provide a means of testing the models developed in this paper on non-standard geometries.

7.1. GEOMETRY

As previously stated, the CTP-FARAD is a frustum. This means that one end has a radius r_1 and the other end has a radius r_2 with a linear slope inbetween. The relation between the local radius and the axial position can therefore be given as Eqn. (7.1). Unlike the MPX or the FRCHX, the current is provided by conductive traces that create a mesh around the frustrum. This mesh can be seen in Figure 7.1. Even though the electric current in each individual trace has both an azimuthal and an axial compoent, the mesh is designed

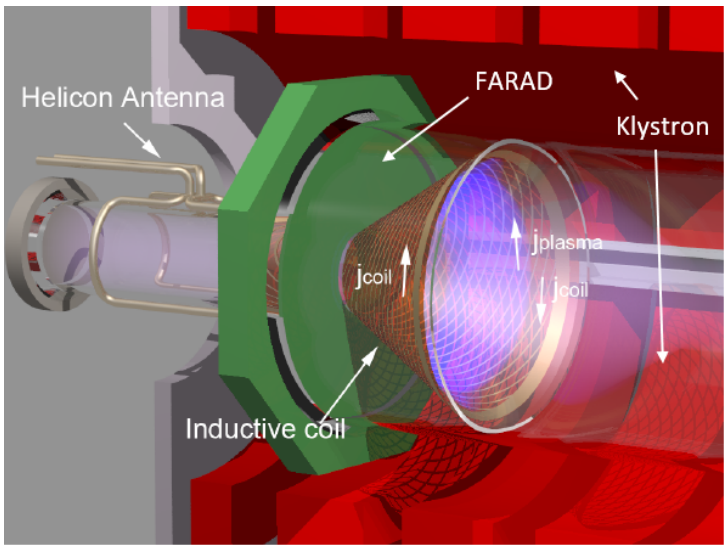

Figure 7.1. Model of the CTP-FARAD mounted on the original FARAD inside a klystron.[33]

overall to cancel out the axial component so that the net current is purely azimuthal. Due to the shape of the frustrum, the current function given in Eqn. (2.16) needs to be changed to account for the radial variance of the conductive traces. The modified equation that will be used for calculating the electric and magnetic fields is as shown in Eqn. (7.2). The change to the radius term from a constant value to a variable value will have the result of changing the integrals with respect to z' in Eqns. (2.17) and (2.18).

$$R(z) = \frac{r_2 - r_1}{L} z + r_1 \tag{7.1}$$

$$f(\vec{r}') = \frac{\delta(r' - R(z'))}{L} \tag{7.2}$$

Eqn. (2.22) remains unchanged and is repeated here as Eqn. (7.3). Eqn. (2.23) is changed to Eqn. (7.4) to reflect the addition of a non-negligible radial field.

$$\vec{E} \approx \partial_t I(t) F_1 \hat{\phi} \tag{7.3}$$

$$\vec{B} \approx I(t)(F_2\hat{r} + F_3\hat{z}) \tag{7.4}$$

The new values of F_1, F_2, and F_3 are given in Eqns. (7.5), (7.6), and (7.7), respectively.

$$F_1 = -\frac{\mu_o}{4\pi}\frac{1}{L}\int_0^{2\pi}\int_0^{L}\frac{R(z')\cos\phi'}{\sqrt{r^2 + R(z')^2 - 2rR(z')\cos\phi' + (z-z')^2}}dz'd\phi' \tag{7.5}$$

$$F_2 = -\frac{\mu_o}{4\pi}\frac{1}{L}\int_0^{2\pi}\int_0^{L}\frac{R(z')(z-z')}{(r^2 + R(z')^2 - 2rR(z')\cos\phi' + (z-z')^2)^{\frac{3}{2}}}dz'd\phi' \tag{7.6}$$

$$F_3 = -\frac{\mu_o}{4\pi}\frac{1}{L}\int_0^{2\pi}\int_0^{L}\frac{R(z')(r\cos\phi' - R(z'))}{(r^2 + R(z')^2 - 2rR(z')\cos\phi' + (z-z')^2)^{\frac{3}{2}}}dz'd\phi' \tag{7.7}$$

The arrangement of the geometry itself varies from iteration to iteration. Initially, the device was mounted on the original FARAD [33]. Thus, the device was placed inside a Varian VA-1955A klystron magnet as shown in Figure 7.1. The klystron served to generate a bias magnetic field that has been reproduced as Figure 7.2. In the CTP-FARAD's final iteration, the klystron was removed and the device was left attached to only a pre-ionization section [45]. In addition, the pre-ionization section was changed from a helicon plasma to a glow discharge in the final iteration [45]. The results analyzed by this work will be for the initial iteration with the klystron magnet and the helicon plasma.

A key result that this work seeks to repeat is the variation of the plasma centroid location with respect to the background gas pressure. Hallock noticed that, as the pressure was increased, the centroid of the plasma would be detected further upstream or toward the small end of the frustrum [33]. A listing of the properties that will be used for the modeling is shown in Table 7.1.

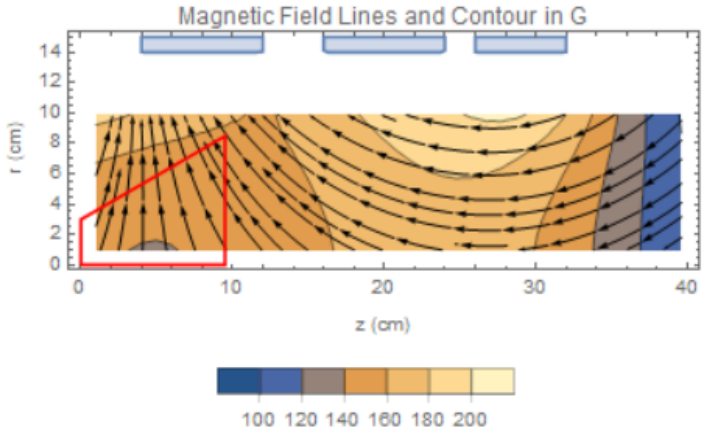

Figure 7.2. Applied bias magnetic field due to the klystron. The outline in red is the acceleration coil.

Table 7.1. Properties for modeling CTP-FARAD.

Chamber Properties		**Gas Properties**	
Coil Min Radius (cm)	4	Gas	Argon
Coil Length (cm)	10	E_{ion} (eV)	15.76
Coil Half-Angle (deg)	20	σ (m^2)	1×10^{-19}
Chamber Material	BN	C_a ($\frac{1}{m \cdot Pa}$)	10.2
Chamber Length (cm)	13.5	C_b ($\frac{V}{m \cdot Pa}$)	176.25
		T (K)	300

7.2. RESULTS

Results for the Single-Particle Model are given in Section 7.2.1 with test parameters given in Table 7.2. Results for the Townsend-Breakdown Model are given in Section 7.2.2.

7.2.1. Single-Particle Model. The challenge with applying the Single-Particle Model to this geometry is the presence of a radial component for the magnetic field. The radial magnetic field component combines with the azimuthal electric field to instill an axial velocity in the electron as shown in Figure 7.3. While the centroid location cannot be easily gleaned from the actions of a single particle, the reduced axial extent of the electron's trajectory at higher pressures presents some qualitative agreement with the expected trend.

Table 7.2. Single-Particle Model parameters for CTP-FARAD.

Simulation Properties	
Time Step (μs)	1×10^{-5}
Number of Time Steps	1×10^{6}
Time Range (μs)	10
Cell Size Min (Radial) (cm)	0.04
Cell Size Max (Radial) (cm)	0.0764
Cell Size (Axial) (cm)	0.1
Number of Cells (Radial)	100
Number of Cells (Axial)	100
Start Position (x) (cm)	2
Start Position (z) (cm)	0.05
Initial Speed (m/s)	0
Test Pressures (mTorr)	5, 10, 20, 30, 40, 50

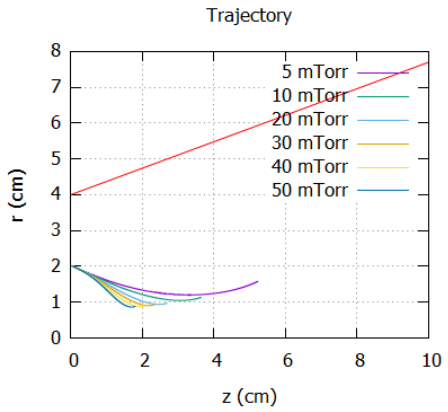

Figure 7.3. Electron trajectory in rz space through the CTP-FARAD. The red diagonal line marks the outer edge of the cone.

However, Figure 7.4 shows that the electron gains very little energy during the range of operation. This severe lack of energy gain may be due to the device being an acceleration coil rather than an ionization coil.

7.2.2. Townsend-Breakdown Model. An image comparing the modeled centroid data to the data obtained by Hallock is shown in Figure 7.5. The model does not in any fashion match the experimental results. Where the experimental results show a strong

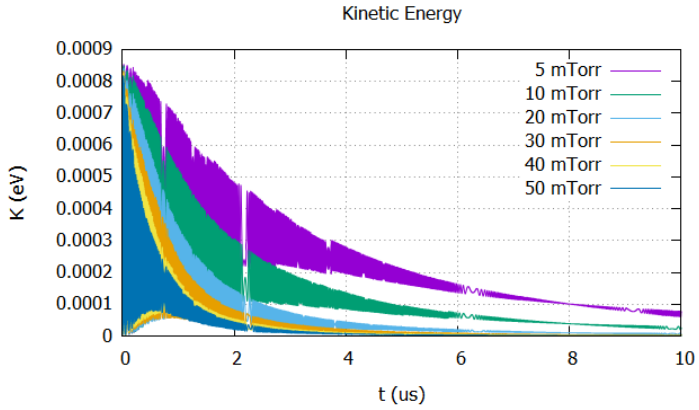

Figure 7.4. Electron kinetic energy in the CTP-FARAD.

degree of variance, the model results remain effectively constant regardless of the pressure. Furthermore, the modeled centroid location is significantly lower than the range found for the experimental results. Reasons for this discrepancy will be discussed in the next section.

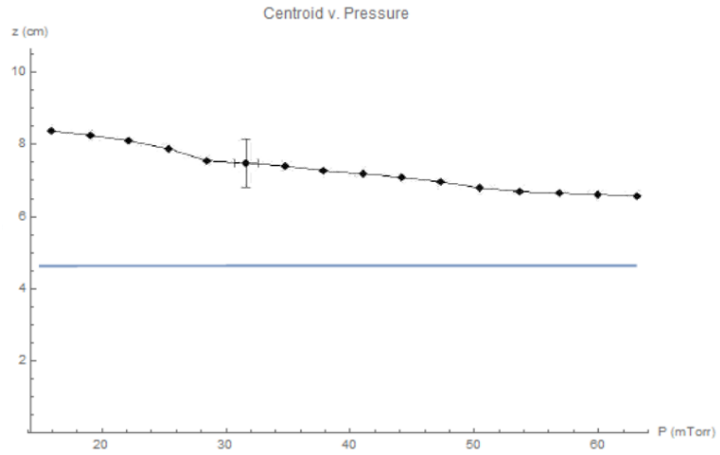

Figure 7.5. Comparison of modeled centroid location and experimental results[33].

7.3. ANALYSIS OF RESULTS

This geometry reveals a key shortcoming in both of my models. Both models assume that no plasma is present in the system throughout the breakdown process and thereby ignore any modifications made to the fields as a result. Thus, while they can describe an ionization coil with a fair degree of accuracy, they cannot in their present state be used to describe sheath formation in an acceleration coil. The reason being that acceleration coils by necessity require the gas to be ionized beforehand as evident by every iteration of the CTP-FARAD making use of a pre-ionizer.

One interesting result that bears discussion is the connection between pressure and centroid position. The shift in centroid presented in the Townsend-Breakdown model result is much smaller in magnitude than the shift presented in Hallock's experimental results. The most likely reason is that the model simply does not handle pressure correctly. The results for both the MPX and FRCHX failed to properly match the pressure relationship so the same is likely true here. Another possible reason for this discrepancy is that, as previously stated, the model does not account for any interactions between the plasma and the fields.

8. SUMMARY AND CONCLUSIONS

8.1. SUMMARY OF WORK

In this work, models were developed to describe formation of inductively-coupled plasmas. First, equations were developed that calculated the electric and magnetic fields as functions of the inductive current. Second, a model was developed that solved the momentum equation for a free electron and then linked plasma formation to the electron's kinetic energy surpassing the ionization energy of the gas. Third, a model was developed that solved the continuity equation for plasma particles generated as a result of Townsend breakdown. Gas breakdown in this model was equated to the maximum of the creation rate rather than a particular threshold value. Finally, these two models were used to simulate plasma formation in three devices: the Missouri Plasmoid Experiment, the Field Reversed Configuration Heating Experiment, and the Conical Theta Pinch - Faraday Acceleration wit Radio-frequency Assisted Discharge. The models matched the results for the first two devices with the exception of the pressure distribution. No agreement was had between the models and the third device.

8.2. CONCLUSION

The derivation of the inductive fields into a form that depends only on the current distribution means that these models can be adapted to any geometry. The work presented in this paper does not show the full extent of that strength as the MPX used solenoidal fields as its baseline and the FRCHX did not give the electric current. Only the CTP-FARAD allowed the strength of the field derivation to show due to its conical geometry. Other geometries that could benefit from the field derivation are the toroidal geometries used by fusion plasmas and the planar geometries used by thrusters. Both models successfully

match the experimental results where plasma formation is coupled to the magnetic field rather than the electric field. The absence of any coupling to the electric field is most evident with the FRCHX results. The highest energies and creation rates are obtained not at the time corresponding to a maximum in the electric field but at a time corresponding to a zero in the magnetic field.

Despite the success of matching the qualitative results, neither model was successful in matching the pressure distributions of the experimental plasmas. The Single-Particle Model took two approaches to incorporating pressure. The first approach was to include pressure in a dampening term. The results of this approach demonstrate a clearly-understandable pattern but do not agree with the nature of an ICP to form a Paschen curve. Instead, the dampening term means peak energies will occur only at the lowest pressures. The second approach was to use pressure to model the distance between hard-body collisions. While the premise is more physically accurate, the results for how it is implemented in this work are essentially gibberish. The Townsend-Breakdown Model used only one approach to pressure. This approach was to combine the pressure with the magnetic field to produce an effective pressure term. It should be noted that the only other attempt to describe an ICP as Townsend-style breakdown did not couple the magnetic field to the pressure value. The weakness of this approach is that the effective pressure term assumes the energy distribution of the system to be Maxwellian and that it can be equated to a similar distribution at a different pressure and no magnetic field.

8.3. FUTURE WORK

There exist two possible routes for future work. First, as previously mentioned, the energy distribution cannot be assumed to be Maxwellian as long as the magnetic field is active and present. However, the distribution can be fairly assumed to be Maxwellian before the system is activated. Thus, work following this route could focus on determining how the energy distribution evolves with time. Ionization could then be read directly from the

distribution function or the change in the distribution could be used to develop a scalable model similar in functionality to the Townsend-breakdown model. The second route is to explore the effect of the capacitive electric field on plasma formation. Both models in their current form assume that ionization is affected only by the inductive electric field. Work following this route could either experimentally isolate the capacitive field and demonstrate the effects held by nullifying it or computationally apply the capacitive field to the plasma models and determine how its addition affects the results.

REFERENCES

[1] Leonard B. Loeb. *Ionization by Collision by Electrons in a Gas*. John Wiley & Sons, Inc., 1939.

[2] James D. Cobine. *Field-Intensified Ionization and Breakdown of Gases*. McGraw-Hill Book Company, Inc, 1941.

[3] K. T. A. L. Burm. Calculation of the townsend discharge coefficients and the paschen curve coefficients. *Contributions to Plasma Physics*, 47(3):177–182, may 2007. doi: 10.1002/ctpp.200710025.

[4] Leonard B. Loeb. *The Second Townsend Coefficient*. John Wiley & Sons, Inc., 1939.

[5] Dragana Marić, Marija Savić, Jelena Sivoš, Nikola Škoro, Marija Radmilović-Radjenović, Gordana Malović, and Zoran Lj. Petrović. Gas breakdown and secondary electron yields. *The European Physical Journal D*, 68(6), jun 2014. doi: 10.1140/epjd/e2014-50090-x.

[6] HA Blevin and SC Haydon. The townsend ionization coefficients in crossed electric and magnetic fields. *Australian Journal of Physics*, 11(1):18, 1958. doi: 10.1071/ph580018.

[7] S N Sen and A K Ghosh. Breakdown of an electrodeless discharge in crossed electric and magnetic fields. *Proceedings of the Physical Society*, 80(4):909–917, oct 1962. doi: 10.1088/0370-1328/80/4/313.

[8] S C Haydon, A I McIntosh, and A A Simpson. The effect of magnetic fields on electron energy distribution functions and derived collision frequencies. *Journal of Physics D: Applied Physics*, 4(9):1257–1265, sep 1971. doi: 10.1088/0022-3727/4/9/304.

[9] Marija Radmilović-Radjenović and Branislav Radjenović. The effect of magnetic field on the electrical breakdown characteristics. *Journal of Physics D: Applied Physics*, 39(14):3002–3009, jun 2006. doi: 10.1088/0022-3727/39/14/019.

[10] P. Chabert and N. Braithwaite. *Physics of Radio-Frequency Plasmas*. Cambridge University Press, 2011.

[11] F F Chen. Plasma ionization by helicon waves. *Plasma Physics and Controlled Fusion*, 33(4):339–364, apr 1991. doi: 10.1088/0741-3335/33/4/006.

[12] O Tarvainen, T Ropponen, V Toivanen, J Ärje, and H Koivisto. Plasma breakdown diagnostics with the biased disc of electron cyclotron resonance ion source. *Plasma Sources Science and Technology*, 18(3):035018, jun 2009. doi: 10.1088/0963-0252/18/3/035018.

[13] Karel Burm. Breakdown magnetic field in an inductively coupled plasma. *Physics Letters A*, 372(41):6280–6283, oct 2008. doi: 10.1016/j.physleta.2008.08.037.

[14] J Hopwood. Review of inductively coupled plasmas for plasma processing. *Plasma Sources Science and Technology*, 1(2):109–116, may 1992. doi: 10.1088/0963-0252/1/2/006.

[15] Seiji Samukawa and Tetsu Mieno. Pulse-time modulated plasma discharge for highly selective, highly anisotropic and charge-free etching. *Plasma Sources Science and Technology*, 5(2):132–138, may 1996. doi: 10.1088/0963-0252/5/2/004.

[16] Seiji Samukawa, Yasuhiro Suzuki, and Masami Sasaki. Extremely high-selective electron cyclotron resonance plasma etching for phosphorus-doped polycrystalline silicon. *Applied Physics Letters*, 57(4):403–405, jul 1990. doi: 10.1063/1.103649.

[17] Seiji Samukawa, Tomohiko Toyosato, and Etsuo Wani. Low radio frequency biased electron cyclotron resonance plasma etching. *Applied Physics Letters*, 58(9):896–898, mar 1991. doi: 10.1063/1.104469.

[18] Nozomi Takeuchi, Koichi Yasuoka, and Shozo Ishii. Surface modification of thin dielectric materials by compact theta-pinch plasma. In *IEEE Conference Record - Abstracts. 2005 IEEE International Conference on Plasma Science*. IEEE, jun 2005. doi: 10.1109/plasma.2005.359142.

[19] W. T. Armstrong. Field-reversed experiments (FRX) on compact toroids. *Physics of Fluids*, 24(11):2068, 1981. doi: 10.1063/1.863303.

[20] W E Quinn and Compact Toroid Staff. Stability and confinement of spheromaks and field reversed configurations. *Physica Scripta*, T2B:391–398, jan 1982. doi: 10.1088/0031-8949/1982/t2b/014.

[21] Y Ono, M Inomoto, Y Ueda, T Matsuyama, and T Okazaki. New relaxation of merging spheromaks to a field reversed configuration. *Nuclear Fusion*, 39(11Y):2001–2008, nov 1999. doi: 10.1088/0029-5515/39/11y/346.

[22] David Kirtley. Study of the synchronous operation of an annular field reversed configuration plasma device, 2008.

[23] M. W. Binderbauer, T. Tajima, L. C. Steinhauer, E. Garate, M. Tuszewski, L. Schmitz, H. Y. Guo, A. Smirnov, H. Gota, D. Barnes, B. H. Deng, M. C. Thompson, E. Trask, X. Yang, S. Putvinski, N. Rostoker, R. Andow, S. Aefsky, N. Bolte, D. Q. Bui, F. Ceccherini, R. Clary, A. H. Cheung, K. D. Conroy, S. A. Dettrick, J. D. Douglass, P. Feng, L. Galeotti, F. Giammanco, E. Granstedt, D. Gupta, S. Gupta, A. A. Ivanov, J. S. Kinley, K. Knapp, S. Korepanov, M. Hollins, R. Magee, R. Mendoza, Y. Mok, A. Necas, S. Primavera, M. Onofri, D. Osin, N. Rath, T. Roche, J. Romero, J. H. Schroeder, L. Sevier, A. Sibley, Y. Song, A. D. Van Drie, J. K. Walters, W. Waggoner, P. Yushmanov, and K. Zhai and. A high performance field-reversed configurationa). *Physics of Plasmas*, 22(5):056110, may 2015. doi: 10.1063/1.4920950.

[24] T. E. Weber, J. T. Slough, and D. Kirtley. The electrodeless lorentz force (ELF) thruster experimental facility. *Review of Scientific Instruments*, 83(11):113509, nov 2012. doi: 10.1063/1.4759000.

[25] Ivana Hrbud, Michael LaPointe, Robert Vondra, C. Lee Dailey, and Ralph Lovberg. Status of pulsed inductive thruster research. In *AIP Conference Proceedings*. AIP, 2002. doi: 10.1063/1.1449781.

[26] Kurt Polzin. Inductive pulsed plasma thruster development and testing at nasa-msfc. In *49th AIAA/ASME/SAE/ASEE Joint Propulsion Conference*, 2013.

[27] Robert Frisbee and Ioannis Mikellides. The nuclear-electric pulsed inductive thruster (nupit): Mission analysis for prometheus. In *41st AIAA/ASME/SAE/ASEE Joint Propulsion Conference and Exhibit*, number AIAA 2005-3892, 2005.

[28] K.A. Polzin. Scaling and systems considerations in pulsed inductive plasma thrusters. *IEEE Transactions on Plasma Science*, 36(5):2189–2198, oct 2008. doi: 10.1109/tps.2008.2003537.

[29] C. Grabowski, J. H. Degnan, D. J. Amdahl, R. Delaney, M. Domonkos, F. M. Lehr, R. Magallanes, P. R. Robinson, E. L. Ruden, W. White, H. Wood, D. Gale, M. Kostora, J. McCullough, W. Sommars, M. H. Frese, S. D. Frese, J. F. Camacho, S. K. Coffey, V. Makhin, T. P. Intrator, G. A. Wurden, J. Sears, P. J. Turchi, W. J. Waganaar, T. Weber, R. E. Siemon, S. Fuelling, B. S. Bauer, A. G. Lynn, and N. F. Roderick. FRC lifetime studies for the field reversed configuration heating experiment (FRCHX). In *2011 IEEE Pulsed Power Conference*. IEEE, jun 2011. doi: 10.1109/ppc.2011.6191459.

[30] Warner Meeks and Joshua Rovey. Numerical and experimental efforts to explain delayed gas breakdown in theta-pinch devices with bias magnetic field. In *48th AIAA/ASME/SAE/ASEE Joint Propulsion Conference & Exhibit*, number AIAA 2012-3929. American Institute of Aeronautics and Astronautics, jul 2012. doi: 10.2514/6.2012-3929.

[31] Francis F. Chen. *Introduction to Plasma Physics and Controlled Fusion*. Springer International Publishing, third ed. edition, 2016. doi: 10.1007/978-3-319-22309-4.

[32] R. J. Goldston and P. H. (Paul Harding) Rutherford. Introduction to plasma physics, 1995. Robert J. Goldston and Paul H. Rutherford., Includes bibliographical references (p. 485-486) and index.

[33] Ashley Hallock, Edgar Choueiri, and Kurt Polzin. Current sheet formation in a conical theta pinch faraday accelerator with radio-frequency assisted discharge. In *44th AIAA/ASME/SAE/ASEE Joint Propulsion Conference & Exhibit*, number AIAA 2008-5201. American Institute of Aeronautics and Astronautics, jul 2008. doi: 10.2514/6.2008-5201.

[34] I. Gimpel and O. Richardson. The secondary electron emission from metals in the low primary energy region. *Proceedings of the Royal Society A: Mathematical, Physical and Engineering Sciences*, 182(988):17–47, sep 1943. doi: 10.1098/rspa.1943.0022.

[35] Adrianus J. Dekker. Secondary electron emission. In *Solid State Physics*, pages 418–445. Prentice Hall, Inc US, 1957.

[36] H. E. Farnsworth. Electronic bombardment of metal surfaces. *Physical Review*, 25 (1):41–57, jan 1925. doi: 10.1103/physrev.25.41.

[37] A.J. Dekker. Secondary electron emission. In *Advances in Research and Applications*, pages 251–311. Elsevier, 1958. doi: 10.1016/s0081-1947(08)60728-6.

[38] S. Mattei, K. Nishida, M. Onai, J. Lettry, M.Q. Tran, and A. Hatayama. A fully-implicit particle-in-cell monte carlo collision code for the simulation of inductively coupled plasmas. *Journal of Computational Physics*, 350:891–906, dec 2017. doi: 10.1016/j.jcp.2017.09.015.

[39] K.T.A.L. Burm. Breakdown minimum in magnetic field-driven metal plasmas. *Journal of Plasma Physics*, 77(05):675–678, feb 2011. doi: 10.1017/s0022377811000067.

[40] R.A. Pahl. Energy deposition into heavy gas plasma via pulsed inductive theta-pinch, 2014.

[41] W.C. Meeks and J.L. Rovey. Argon and xenon pulsed theta-pinch plasma via optical emission spectroscopy. In *33rd International Electric Propulsion Conference*, number IEPC-2013-378. IEEE, October 2013.

[42] Ryan Pahl and Joshua Rovey. Pre-ionization plasma in an FRC test article. In *50th AIAA Aerospace Sciences Meeting including the New Horizons Forum and Aerospace Exposition*, number AIAA 2012-0194. American Institute of Aeronautics and Astronautics, jan 2012. doi: 10.2514/6.2012-194.

[43] Ryan A. Pahl and Joshua L. Rovey. Effects of DC preionization voltage and radial location on pulsed inductive plasma formation. *IEEE Transactions on Plasma Science*, 43(11):3883–3888, nov 2015. doi: 10.1109/tps.2015.2484319.

[44] Edgar Y. Choueiri and Kurt A. Polzin. Faraday acceleration with radio-frequency assisted discharge. *Journal of Propulsion and Power*, 22(3):611–619, may 2006. doi: 10.2514/1.16399.

[45] A.K. Hallock. Effect of inductive coil geometry on the operating characteristics of a pulsed inductive plasma, 2012.

[46] Matthew S Feldman and Edgar Y Chouieri. Single stage faraday accelerator with radio-frequency assisted discharge (ss-farad). In *32nd International Electric Propulsion Conference*, number IEPC-2011-220, 2011.

VITA

Zachary Gill was born and raised in Tulsa, OK. In May of 2011, he graduated from Booker T. Washington High School ranked near the top of his class. He then attended The University of Tulsa as a recipient of the Unit Corp. Presidential Scholarship. In May of 2015, he graduated Magna Cum Laude with a B.S. in Engineering Physics, a concentration in Electro-Optical Communications, and a minor in Mathematics.

Zachary then enrolled in the Direct-Ph.D. program at the Missouri University of Science and Technology. He was a recipient of the Chancellor's Distinguished Fellowship and conducted his research with the Aerospace Plasma Lab and then the Gas and Plasma Dynamics Laboratory. He received the Master of Science in Aerospace Engineering from Missouri S&T in December 2018.

In the summer of 2017, Zachary worked as a Summer Scholar for the Air Force Research Lab. His work focused on verifying the efficacy of computer-assisted RF compensation of a Langmuir probe. He presented a poster at the 59th Annual Meeting of APS-DPP.